remote sensing

MDPI

Article

Characterization of Fresh and Aged Smoke Particles Simultaneously Observed with an ACTRIS Multi-Wavelength Raman Lidar in Potenza, Italy

Benedetto De Rosa [1,*], Aldo Amodeo [1], Giuseppe D'Amico [1], Nikolaos Papagiannopoulos [1], Marco Rosoldi [1], Igor Veselovskii [2], Francesco Cardellicchio [1], Alfredo Falconieri [1], Pilar Gumà-Claramunt [1], Teresa Laurita [1], Michail Mytilinaios [1], Christina-Anna Papanikolaou [1], Davide Amodio [1], Canio Colangelo [1], Paolo Di Girolamo [3], Ilaria Gandolfi [1], Aldo Giunta [1], Emilio Lapenna [1], Fabrizio Marra [1], Rosa Maria Petracca Altieri [1], Ermann Ripepi [1], Donato Summa [1], Michele Volini [1], Alberto Arienzo [1] and Lucia Mona [1]

[1] Consiglio Nazionale delle Ricerche—Istituto di Metodologie per l'Analisi Ambientale CNR-IMAA, 85050 Potenza, Italy; aldo.amodeo@cnr.it (A.A.); giuseppe.damico@cnr.it (G.D.); nikolaos.papagiannopoulos@cnr.it (N.P.); marco.rosoldi@cnr.it (M.R.); francesco.cardellicchio@cnr.it (F.C.); alfredo.falconieri@cnr.it (A.F.); pilar.gumaclaramunt@cnr.it (P.G.-C.); teresa.laurita@cnr.it (T.L.); michail.mytilinaios@cnr.it (M.M.); christinaannapapanikolaou@cnr.it (C.-A.P.); davide.amodio@cnr.it (D.A.); canio.colangelo@cnr.it (C.C.); ilaria.gandolfi@cnr.it (I.G.); aldo.giunta@cnr.it (A.G.); emilio.lapenna@cnr.it (E.L.); fabrizio.marra@cnr.it (F.M.); rosamaria.petraccaaltieri@cnr.it (R.M.P.A.); ermann.ripepi@cnr.it (E.R.); donato.summa@cnr.it (D.S.); michele.volini@cnr.it (M.V.); alberto.arienzo@cnr.it (A.A.); lucia.mona@cnr.it (L.M.)

[2] Physics Instrumentation Center of General Physics Institute, Troitsk, 119991 Moscow, Russia; igorv@pic.troitsk.ru

[3] Dipartimento di Scienze della Salute, Università degli Studi della Basilicata, 85100 Potenza, Italy; paolo.digirolamo@unibas.it

* Correspondence: benedetto.derosa@cnr.it

check for updates

Academic Editor: Massimiliano Pepe

Received: 4 June 2025
Revised: 10 July 2025
Accepted: 19 July 2025
Published: 22 July 2025

Citation: De Rosa, B.; Amodeo, A.; D'Amico, G.; Papagiannopoulos, N.; Rosoldi, M.; Veselovskii, I.; Cardellicchio, F.; Falconieri, A.; Gumà-Claramunt, P.; Laurita, T.; et al. Characterization of Fresh and Aged Smoke Particles Simultaneously Observed with an ACTRIS Multi-Wavelength Raman Lidar in Potenza, Italy. *Remote Sens.* **2025**, *17*, 2538. https://doi.org/10.3390/rs17152538

Abstract

This study describes a quite special and interesting atmospheric event characterized by the simultaneous presence of fresh and aged smoke layers. These peculiar conditions occurred on 16 July 2024 at the CNR-IMAA atmospheric observatory (CIAO) in Potenza (Italy), and represent an ideal case for the evaluation of the impact of aging and transport mechanisms on both the optical and microphysical properties of biomass burning aerosol. The fresh smoke was originated by a local wildfire about 2 km from the measurement site and observed about one hour after its ignition. The other smoke layer was due to a wide wildfire occurring in Canada that, according to backward trajectory analysis, traveled for about 5–6 days before reaching the observatory. Synergetic use of lidar, ceilometer, radar, and microwave radiometer measurements revealed that particles from the local wildfire, located at about 3 km a.s.l., acted as condensation nuclei for cloud formation as a result of high humidity concentrations at this altitude range. Optical characterization of the fresh smoke layer based on Raman lidar measurements provided lidar ratio (LR) values of 46 ± 4 sr and 34 ± 3 sr, at 355 and 532 nm, respectively. The particle linear depolarization ratio (PLDR) at 532 nm was 0.067 ± 0.002, while backscatter-related Ångström exponent (AEβ) values were 1.21 ± 0.03, 1.23 ± 0.03, and 1.22 ± 0.04 in the spectral ranges of 355–532 nm, 355–1064 nm and 532–1064 nm, respectively. Microphysical inversion caused by these intensive optical parameters indicates a low contribution of black carbon (BC) and, despite their small size, particles remained outside the ultrafine range. Moreover, a combined use of CIAO remote sensing and in situ instrumentation shows that the particle properties are affected by humidity variations, thus suggesting a marked particle hygroscopic behavior. In contrast, the smoke plume from the Canadian wildfire traveled at

altitudes between 6 and 8 km a.s.l., remaining unaffected by local humidity. Absorption in this case was higher, and, as observed in other aged wildfires, the LR at 532 nm was larger than that at 355 nm. Specifically, the LR at 355 nm was 55 ± 2 sr, while at 532 nm it was 82 ± 3 sr. The AEβ values were 1.77 ± 0.13 and 1.41 ± 0.07 at 355–532 nm and 532–1064 nm, respectively and the PLDR at 532 nm was 0.040 ± 0.003. Microphysical analysis suggests the presence of larger, yet much more absorbent particles. This analysis indicates that both optical and microphysical properties of smoke can vary significantly depending on its origin, persistence, and transport in the atmosphere. These factors that must be carefully incorporated into future climate models, especially considering the frequent occurrences of fire events worldwide.

Keywords: fresh biomass burning; aged biomass burning; smoke; Raman lidar; relative humidity

1. Introduction

Biomass burning events have a significant effect on the chemical composition of the atmosphere, leading to the emission of large quantities of aerosols and greenhouse gases. Emitted particles may have significant impacts on air quality and human health. Smoke from wildfires includes chemical components severely degrading air quality and causing health risks [1,2]. For example, human exposure to wildfire smoke may lead to respiratory and cardiovascular diseases, as fine particles can extensively penetrate the lungs and be deposited in the airways or alveoli, with the extent of penetration depending on particle size and microphysical properties [3].

Atmospheric particles from biomass burning and wildfire events also play a significant role in shaping weather and climate patterns. These events are associated with the capability of altering radiative forcing at both regional and global scales [4]. Wildfires are considered a major contributor to the overall atmospheric aerosol load, particularly during fire seasons. It is estimated that biomass burning accounts for approximately 30% of global aerosol emissions [5].

A comprehensive characterization of the impact of aerosols from biomass combustion on climate remains difficult. Particle direct radiative effects can be both positive and negative due to the opposing influences of their two main components: black carbon (BC) and organic carbon (OC). BC is highly absorbing, thus causing a positive radiative effect, while OC primarily scatters light, leading to a negative radiative effect [5,6]. In large wildfires, high temperatures may favor more efficient combustion processes, leading to higher BC concentrations [7,8]. Furthermore, when absorbing aerosols, such as BC, interact with purely scattering aerosols, additional complexities arise. One notable scenario is the internal mixing of BC with scattering aerosols, which are possibly in biomass-burning and fossil fuel emissions. This mixing can enhance BC absorption by a factor of 1 to 2.5, depending on the structure and morphology of the mixture [9].

Additionally, aerosol particles emitted by biomass burning may indirectly modulate cloud microphysics by serving as cloud condensation nuclei (CCN) or ice nucleating particles (INPs). CCN promote liquid cloud droplet formation, enhancing cloud albedo and leading to a cooling effect. INPs, instead, facilitate ice crystal formation in supercooled clouds, influencing cloud lifetime and precipitation. Given the distinct role of CCN and INPs in cloud formation mechanisms, additional complexity is added to the assessment of wildfire aerosols on climate [10].

During its transport, wildfire smoke undergoes aging processes, including coagulation, oxidation, and condensation [11]. Such processes affect particle morphology, size distribution, and chemical composition, often resulting in diminished absorptive efficiency [12] due to secondary material coating and structural changes [13,14].

Studies have shown that fire plumes can traverse the Atlantic Ocean, significantly influencing air quality and climate across continents [15–17]. In this context, the establishment of the EARLINET lidar network [18] has been crucial for characterizing these smoke plumes at the continental level and understanding their impact on the atmosphere [19].

While extensive research has focused on large wildfires, especially in terms of their optical and microphysical properties, there is a notable gap in the study of smoke from smaller fires, and their possible influence on boundary-layer aerosol dynamics and cloud processes. For the few cases reported in the literature, the fraction of BC [20,21] is typically lower than the one characterizing large wildfires.

Notably, although characterized by lower emission intensities and spatial extents, small wildfires occur with high frequency and represent a non-negligible source of atmospheric aerosols on a global scale. In many cases, the plumes from these smaller fires remain undetected by satellite-based sensors due to their limited spatial resolution. As a consequence, their contribution to the atmospheric radiative budget is frequently overlooked or underestimated, emphasizing the necessity of ground-based observations to accurately assess their true impact [22,23]. Some studies have shown that even small wildfires can trigger cloud formation, as a result of aerosol particles acting as CCN [24,25]. However, the interaction between wildfire aerosols and cloud microphysics is a complex and still poorly understood process, especially for small-scale fires. The exact nature of these mechanisms is highly dependent on local atmospheric conditions, including humidity and temperature. For instance, in regions with high humidity, even relatively large and less hygroscopic particles can act as CCN, potentially leading to the formation of small, short-lived clouds [26,27], as observed in this study. Furthermore, although still poorly studied, the interactions between aerosols and clouds in small wildfires are particularly significant due to their potential to modify the local radiation budget [28–30].

In this context, active remote sensing techniques, with their high temporal and vertical resolutions, are valuable tools for quantifying and monitoring these changes in aerosol properties, allowing for more accurate modeling of the impact of wildfires on the climate system and at regional and global scales.

In this study, we focus on multi-wavelength lidar measurements carried out in Potenza, Italy, on 16 July 2024 aimed at characterizing the optical and microphysical properties of smoke particles from two distinct wildfire events: one ignited locally, and one ignited in Canada, the latter having experienced long-range oversea transport.

The present study addresses a significant gap in the literature by offering a concurrent observational comparison of the optical and microphysical characteristics of both locally ignited and long-range transported wildfire events.

Unlike previous studies focused primarily on large wildfires, this analysis emphasizes the unique features of emissions from smaller fires, their role in cloud formation, and their implications for climate dynamics. Consequently, this study provides novel insights that are essential for refining climate models and improving aerosol radiative forcing estimates.

These findings offer quantitative constraints on key aerosol properties, such as size distribution, chemical composition, and hygroscopic growth factors, which can be directly integrated into global climate model parameterizations. Specifically, the observed variability in aerosol optical properties across different atmospheric regimes provides critical input for refining aerosol radiation and aerosol cloud interaction schemes. Implementing these empirically derived parameters in Earth system models can reduce the uncertainty

in aerosol radiative forcing estimates, especially for short-lived climate forcers. Future modeling efforts should aim to assimilate these observational constraints to evaluate their influence on climate sensitivity and long-term projections.

This paper is structured as follows: Section 2 provides a detailed description of the instrumentation used in this study, including its technical specifications and operational settings. Section 3 presents an overview of the case study, focusing on the characterization and origin of the two distinct aerosol layers detected during the observations. In Section 4, the characterization of the local and the Canadian wildfire is reported using a multisensory approach. At the end of the section, the optical and microphysical properties of the two smoke plumes were compared. Conclusions are reported in Section 5.

2. Materials and Methods

The measurements presented in this paper were collected at the CNR-IMAA Atmospheric Observatory (CIAO) [31–33]. CIAO is located in the heart of the Mediterranean Basin on the Apennine Mountains (40.60°N, 15.72°E, 760 m above sea level), and has operated since 2000. CIAO serves as a strategic site for studying a wide variety of aerosol types under diverse meteorological conditions, influenced by both Mediterranean atmospheric circulation and regional orography. Its location, less than 150 km from both the Tyrrhenian and Ionian Seas, enhances its capability to effectively monitor aerosol dynamics. Additionally, CIAO is situated near forested areas, allowing for the observation of local wildfires, particularly during the dry and hot summer months when such events are more likely to occur [20]. This makes CIAO an invaluable and strategic site for the characterization of aerosol properties.

Since the early 2000s, CIAO has been committed to providing long-term aerosol remote sensing observations. CIAO was a core member of the European Aerosol Research Lidar Network (EARLINET), established in 2000 with the aim of creating a harmonized network of lidar stations in Europe to study the vertical distribution of aerosols. The site has always been among the pillars of EARLINET for the quality and continuity of observations, as well as for methodological and instrumental development.

Today, the observatory has a relevant role in ACTRIS [34] (Aerosol, Clouds, and Trace Gases Research Infrastructure, https://www.actris.eu, accessed on 11 April 2025). ACTRIS is a European Research Infrastructure (RI) for the characterization of aerosols, clouds, and trace gases using and integrating remote sensing and in situ observations, and experimental platforms for the characterization of atmospheric components. CIAO, combining a multitude of aerosol remote sensing and in situ sensors, allows for multidimensional and in-depth studies.

Currently, CIAO is the Italian node of the ACTRIS Central Facility CARS (Centre for Aerosol Remote Sensing), which provides services to users as well as operation support to all the ACTRIS National Facilities (NFs) operating aerosol remote sensing instruments. The Potenza Lidar for Particle Observation (POLPO) is not only an observational platform of ACTRIS, but also one of the ACTRIS reference lidar systems operative of CARS, established to test and calibrate high-power lidar systems through direct intercomparison. The system significantly surpasses the baseline requirements for National Facilities, offering enhanced performance and an extended range of measurable atmospheric parameters.

All the instruments involved in this study are listed in Table 1.

Table 1. List of all the instruments used for this study.

Instrument	Main Products
Raman Lidar (POLPO—Potenza Lidar for Particle Observation)	Aerosol backscatter @1064, 532 and 355 nm Aerosol depolarization ratio @1064, 532 and 355 nm Aerosol extinction @532 and 355 nm Water vapor mixing ratio
Doppler Radar (MIRA35—METEK)	Doppler spectrum Doppler velocity Linear Depolarization Ratio
Ceilometer (CL51—VAISALA)	Aerosol backscatter Cloud base height
Microwave Radiometer (RPG-HATPRO-G5—Radiometer Physics)	Temperature, humidity and cloud liquid water profiles Integrated Precipitable Water Vapor (IPWV) Cloud Liquid Water Path (LWP)
ACSM	Chemical composition and mass (<1 μm)
Aethalometer AE33	Black Carbon (BC) concentration

2.1. Multi-Wavelength Raman Lidar POLPO

POLPO is strategically located within a thermally insulated container, and is integrated with a dedicated ground weather station, enabling continuous monitoring of local atmospheric conditions during measurements. This advanced lidar system is designed for remote control via internet access, ensuring flexible operation and facilitating easy access to the collected data. To maintain the reliability of the measurements, the system automatically suspends data collection in the event of rain, resuming operations after a 10 min interval, which is crucial for avoiding measurements that may be compromised by adverse weather conditions. The POLPO lidar incorporates two distinct laser sources, both of them emitting linearly polarized pulses. The first laser emits exclusively at 1064 nm, in order to avoid loss of polarization purity due to second and third harmonic crystal generators, allowing for enhanced measurements of aerosol depolarization at this wavelength, with a single-pulse energy output of 150 mJ, a repetition frequency of 20 Hz, and a divergence of less than 1.2 mrad. The second laser emits pulses with an energy of 200 mJ at 355 nm and 100 mJ at 532 nm, operating at a repetition frequency of 10 Hz, with beam divergence being less than 1.2 mrad for all wavelengths.

From a ray-tracing analysis, the system is equipped with two telescopes, one for measurements in the far-range (classical Cassegrain telescope with a primary mirror diameter of 400 mm), and the other for measurements in the near-range (Dall–Kirkham telescope with a primary mirror diameter of 200 mm). The gluing of the signals measured by two telescopes allows us to highly extend the detected dynamic range, spanning from about 200 m (full overlap height of the near-range telescope) up to about 25 km (considering the far-range telescope) with a good linearity and signal to noise ratio.

Cross and parallel polarization components at all wavelengths are detected individually, being separated through a beam splitter polarizing cube. Detection is performed through photomultiplier tubes, except for 1064 nm, which is detected by means of an APD. The backscattered radiation at all the wavelengths is acquired in both analogical and photon counting mode, except for 1064, which is acquired only in analogical mode. The lidar respects all the Standard Operation Procedures (SOPs) implemented by ACTRIS for the high-power lidar. Specifically, SOPs refer to the full set of quality assurance (QA) tests that are submitted every two months to ensure that the system complies with the high standards required by ACTRIS. These tests typically include telecover tests, Rayleigh fit analysis, polarization calibration, zero bin determination, and dark signal measurement [35–37] (https://www.actris.eu/sites/default/files/inline-files/SOPs-CARS-Nov2023-v01-rev08.pdf, accessed on 11 April 2025). POLPO performs continuous measurements of aerosol backscat-

tering coefficients at 355 nm, 532 nm, and 1064 nm, aerosol extinction coefficients at 355 nm and 532 nm, volume and particle depolarization ratios at 355 nm, 532 nm, and 1064 nm, and water vapor mixing ratio assessment in both the planetary boundary layer (PBL) and the free troposphere. The advanced capabilities of the POLPO system make it an important tool for characterizing atmospheric properties and studying aerosols, significantly contributing to research in atmospheric science and environmental monitoring. The data are centrally processed [38], curated, and made available by the ACTRIS ARES (Aerosol Remote Sensing) Data Centre. Data products available include pre-processed lidar data (a step further undertaken for raw data, including all instrumental corrections and harmonizations), cloudmasking, aerosol optical properties profiles, combined lidar–photometer products, and climatological products. Data are available at the ACTRIS data portal at https://dc.actris.nilu.no (accessed on 18 January 2025) and at the specialized ACTRIS/EARLINET database at https://data.earlinet.org (accessed on 18 January 2025).

2.2. Radar, Ceilometer, and Microwave Radiometer

The CIAO ACTRIS observational platform is also equipped with the cloud remote sensing component, including various instruments, such as a mono-static Ka-band Doppler radar, a ceilometer, and a multi-channel microwave radiometer, all operating continuously and automatically.

The radar (Metek, model: MIRA35) has a 1 m diameter antenna vertically emitting linear polarized microwave pulses at 35.5 GHz, with a peak power of 30 kW, duration of 200 ns, repetition rate of 5 KHz, and beam width of 0.6°. Parallel and cross polarized backscattered radiation from atmospheric particles is detected to provide the tropospheric profiles of their Doppler spectrum and related moments. The atmospheric particles detectable by the radar are the hydrometeors forming clouds and precipitations, as well as insects and giant aerosols [39,40]. The retrieved Doppler spectrum's moments are the signal-to-noise ratio (SNR), the mean Doppler velocity, the Doppler spectrum peak width, and the equivalent reflectivity factor Ze, which depends on the particle size distribution. Moreover, the ratio of SNRs measured in the cross and parallel channels, or the linear depolarization ratio (LDR), is also provided, which depends on particles' asphericity. The contributions to the Doppler spectrum and moments of non-meteorological targets (insects and giant aerosols) are separated from those of hydrometeors and filtered, while all radar profiles are provided with vertical and time resolution of 30 m and 10 s, respectively.

The ceilometer (Vaisala, model: CL51) employs an eye-safe diode laser transmitter, emitting short light pulses at 910 $\pm$ 10 nm, with energy of ~3 µJ, duration of ~110 ns, repetition frequency of 6.5 kHz, and beam divergence of 0.15 $\times$ 0.25 mrad, in the near-zenith direction and using a single-lens trans-receiver. The elastic backscattered radiation from aerosol particles and cloud hydrometeors is detected by an avalanche photodiode receiver with a 0.56 mrad field of view, providing the attenuated backscatter coefficient profiles for the continuous characterization and monitoring of aerosols and clouds' vertical layering through the troposphere, as well as for the detection of fog layers and precipitation [41,42]. The ceilometer profiles have vertical and time resolutions of 10 m and 30 s, respectively.

The microwave radiometer (Radiometer Physics GmbH, model: RPG-HATPRO-G5) measures the sky brightness temperature at 14 frequencies: 7 in the K-band, among which 6 are distributed from the center onto the wing of the 22 GHz water vapor resonance absorption line (22–28 GHz), and one at 31.4 GHz; the rest are in the V-band, distributed on one shoulder of the 60 GHz oxygen spin-rotation band (51–58 GHz). Although the measurements are mainly performed in the zenith direction, the radiometer is equipped with azimuth and elevation positioners for full sky scanning. From brightness temperature (Tb) measurements, various atmospheric parameters can be retrieved, using neural network al-

gorithms trained by forward modeling ingesting several years of historical radio-soundings data [43,44]. From zenith measurements of Tbs in the K-band, the column-integrated water vapor (IWV) and the cloud-integrated liquid water, or liquid water path (LWP), as well as tropospheric profiles of humidity, are retrieved. From zenith measurements of Tbs in the V-band, tropospheric temperature profiles are retrieved. In addition, Tbs are also measured during elevation scans performed every 15 min, which improve the vertical resolution of temperature profiles in the boundary layer. The microwave radiometer is also equipped with an infrared radiometer (spectral range 9.6–11.5 μm), which measures the Tb of cloud base (if any) and allows estimation of the cloud base height using the temperature profile. IWV and LWP are provided with a time resolution of 1 s, while temperature and humidity profiles are provided with a time resolution of 1 min and vertical resolutions in the range 25–300 m, decreasing as the altitude increases.

Data from the above instruments, combined with those derived from ECMWF models, are processed by the ACTRIS Cloud Remote Sensing Data Centre Unit (CLU) using Cloudnet algorithms and software [45,46], allowing height-resolved discrimination between aerosols, insects, and the different types of hydrometeors (liquid droplets, ice crystals, drizzle, and rain), and the retrieval of cloud geometrical and microphysical properties, such as the height of cloud base and top, profiles of ice water content, and liquid water content. Cloudnet products have time and vertical resolution of 30 s and 30 m, respectively, and are available, together with source instrumental data, on the Cloudnet data portal (https://cloudnet.fmi.fi, accessed on 11 April 2025) and on the ACTRIS data portal (https://data.actris.eu, accessed on 11 April 2025).

2.3. Aethalometer and ACSM

CIAO is also an ACTRIS aerosol in situ observational platform. The aerosol instrumentation and the laboratory setup follow the ACTRIS recommendations for aerosol sampling, measurement, and analysis (https://www.actris-ecac.eu/measurement-guidelines.html, accessed on 11 April 2025). As the in situ component is a newly established ACTRIS National Facility observation platform for aerosol observations and is currently undergoing the official ACTRIS labeling process, the data collected by these instruments are not yet available through ACTRIS public data portals.

The in situ aerosol facility at CIAO is equipped with a comprehensive set of advanced instruments for real-time monitoring of the physical and chemical properties of atmospheric aerosol particles [32]. Among these, the Aethalometer AE33-Dual Spot (Magee Scientific) and the time-of-flight aerosol chemical speciation monitor (ToF-ACSM, Aerodyne Research) are of particular relevance to the present study.

The Aethalometer AE33-Dual Spot, operating at seven different wavelengths in the range of 370–950 nm, is used for the real-time detection of a light-absorbing particulate component, known as BC, formed during the incomplete combustion of carbonaceous matter from biomass burning and fossil fuel.

Among the in situ aerosol instruments, the Aethalometer is particularly valuable for studying smoke from wildfires. It provides quantitative measurements of BC originating from the incomplete combustion of carbonaceous matter and enables an estimation of the contribution of biomass burning to the overall BC levels [47,48].

The Aethalometer is connected to the PM10 common inlet (shared with the Aerodynamic Particle Sizer and Nephelometer) and is equipped with a sample stream dryer (Magee Scientific) exploiting a semi-permeable Nafion membrane, which keeps the RH well below 40%. These environmental conditions, besides preventing possible instrument damage caused by water condensation, also avoid the interaction of water with aerosol

species, thus preventing changes in their physical and optical properties and inaccuracies in the determination of BC content.

The ToF-ACSM is installed at the CIAO observatory for real-time characterization of atmospheric aerosols. Based on the technology of Aerosol Mass Spectrometers (AMSs) [49,50], the ToF-ACSM is designed to provide continuous and reliable measurements of the non-refractory fraction of fine particulate matter (NR-PM1). Its ability to operate autonomously over extended periods makes it ideal for environmental studies and air quality monitoring.

The chemical composition of NR-PM1 includes the quantification of the organic aerosol fraction (OA) and inorganic components such as NH_4^+, NO_3^-, SO_4^{2-}, and Cl^-. Thanks to its ability to identify and quantify both organic and inorganic components in the air, the ToF-ACSM is an essential instrument for studying particles emitted during combustion. By applying Positive Matrix Factorization (PMF) to the collected data, it is possible to distinguish between different sources of organic compounds, including biomass burning. This approach proves crucial for monitoring the temporal and spatial evolution of aerosol chemical composition.

3. Results

This study takes advantage of a unique atmospheric condition observed on 16 July 2024, enabling a comparative analysis of two smoke plumes originating from different sources. Typically, the remote sensing of wildfire smoke layers is challenging due to their episodic nature and variability in transport dynamics. However, during our observation on 16 July 2024, a unique atmospheric scenario occurred, allowing us to distinguish and compare two separate smoke plumes at different altitudes, each originating from a different source.

The lidar measurements of total attenuated backscatter coefficient at 1064 nm (Figure 1) clearly show the presence of a lower layer, extending from the surface up to approximately 3 km of altitude a.s.l., and a secondary, thinner layer visible between 6 and 8 km.

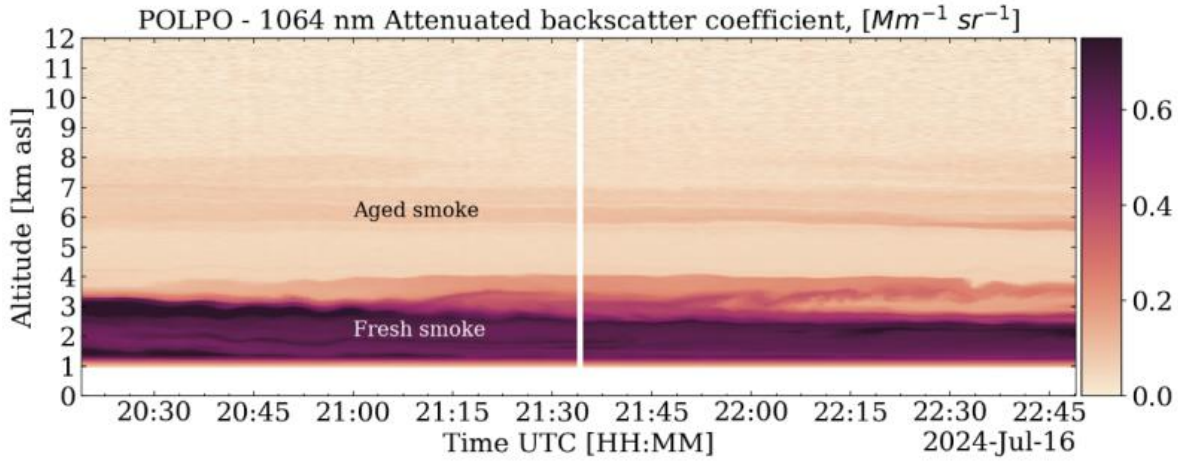

Figure 1. Temporal evolution of the 1064 nm total attenuated backscatter coefficient obtained with the POLPO system on 16 July 2024, 20:19–22:50 UTC.

Origin of the Two Observed Layers

The first observed layer is attributable to a local wildfire. On 16 July 2024, around 15:00 UTC, a fire started on a hill located 2 km from the CIAO observatory and was totally under the control of the local fire brigade at about 22:00 UTC.

The burned forests belong to the category of mesophilic and meso-thermophilic oak woods, primarily characterized by Turkey oak (*Quercus cerris*). These forests represent one of the most extensive forest formations in Basilicata, dominating the region's hilly and

mountainous landscape [51]. The extent of the burnt area and the location of CIAO can be seen in Figure 2, the former being estimated based on data from MSI (MultiSpectral Instrument) onboard the Copernicus Sentinel-2. Specifically, we used MSI Level 2 data in the short-wave infrared (SWIR) for a pre-fire and post-fire satellite overpass (i.e., 15 July 2024 at 00:00 UTC and 17 July 2024 at 00:00 UTC).

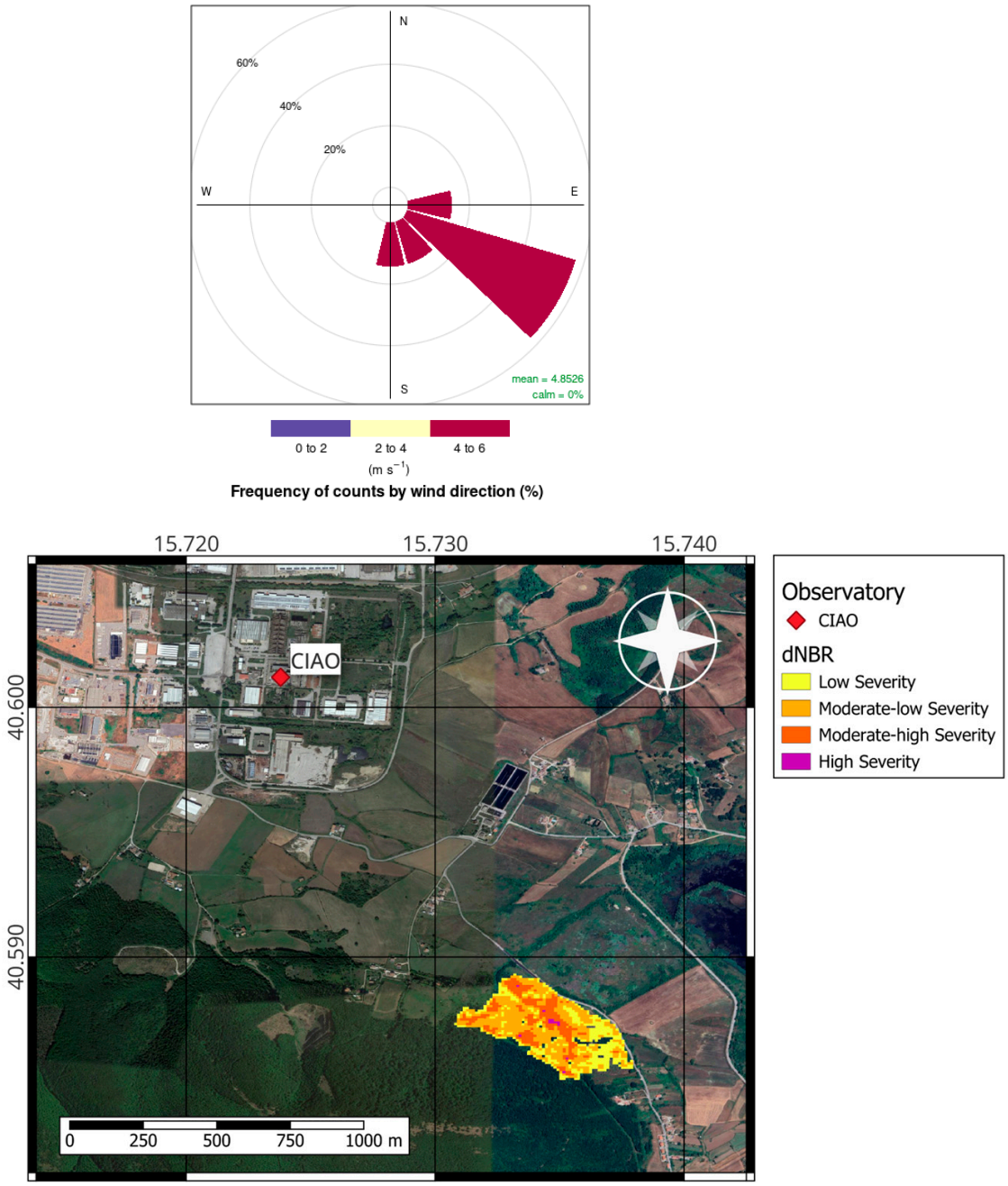

Figure 2. The figure shows the wind rose created using the U and V wind components at 650 hPa from ERA5 reanalysis data, the location of CIAO and the extent of the burnt area. The latter is estimated from MSI/Sentinel-2 SWIR data, which indicate the burnt oak forest fire on 16 July 2024 near the CIAO observatory.

Newly burned land reflects strongly in SWIR bands, making them valuable for mapping fire damages. The burned area shown in the figure covers approximately 20 hectares and is located 1.6 km southeast of CIAO. In addition, the wind rose in the figure indicates prevailing winds from the southeast and a speed of 4–6 m/s. These support the transport of

smoke from the fire area toward the observatory. The smoke from the wildfire corresponds to the low-altitude layer observed in Map 1. Obviously, the layer present at 7 km must have a different origin.

The back-trajectory analysis at 6.5 km reveals that these aerosols originated in Canada. Canada's frequent wildfires result from its vast boreal forests, where dry conditions and lightning strikes are common ignition sources. Climate change has amplified the risk, leading to increased fire frequency and severity due to rising temperatures, prolonged droughts, and a reduced snowpack in spring. These factors create a more fire-prone environment, as documented by several studies [52,53]. In 2024 alone, 6551 wildfires burned 15 million hectares of land, making it the most destructive fire season in the country's history [52].

The wildfires in Canada during 2024 continued the unprecedented trend set by the record-breaking fires of 2023 [53]. These smoke plumes severely impacted air quality, not only across Canada and the United States, but also as far as Mexico and Europe [53]. The 2024 wildfire season was on track to be the second highest in terms of carbon emissions since the Copernicus Atmosphere Monitoring Service began recording data in 2003, surpassed only by the devastation of 2023. The total area affected by the fires exceeded 5.3 million hectares (13 million acres), making it one of the six worst fire years in the past half-century [53].

The satellite maps accurately delineate the spatial distribution of smoke from a major wildfire in Canada, which was most probably responsible for the long-range transported smoke observed and reported in this paper. Figure 3a highlights the smoke plume in red via an unsupervised k-means classification technique. Data for visualizing the smoke plume were obtained from the Sentinel-3 OLCI sensor during consecutive overpasses over Canada at 17:00, 18:00, and 19:00 UTC on 10 July 2024. Figure 3b shows a false-color representation using Sentinel-3 OLCI bands 17 (865 nm), 6 (560 nm), and 3 (490 nm), which effectively emphasizes the smoke in shades of gray and brown.

Figure 3c integrates backward trajectories, illustrated in blue, computed with the HYSPLIT [54,55] model starting at 20:00 UTC on 16 July 2024 at an altitude of 6.5 km above CIAO, and tracing back for a period of six days to identify origins of the air masses involved with the smoke dispersion. The delineated area in yellow enhances the visualization of the specific region being analyzed, providing detailed views of the smoke dispersion. Figure 3d illustrates the trajectory heights as a function of time.

A clear laminar motion is observed. Indeed, when the energy of large wildfires is insufficient to transport smoke into the stratosphere, aerosols remain within the free troposphere. Larger particles tend to settle due to gravitational forces, while smaller particles are influenced by two opposing forces. Gravity drives them downward, while, simultaneously, the absorption of electromagnetic radiation by their BC component leads to heating, inducing an upward motion. When these forces reach equilibrium, a laminar flow can develop, allowing highly absorbing aerosols to persist in the troposphere for several days [15]. Overall, tropospheric aerosols from wildfires tend to be smaller and more spherical, contributing to a stronger warming direct effect [15].

The laminar motion in the figure appears more pronounced over the ocean, likely due to lower atmospheric turbulence. Over oceanic surfaces, the absence of orographic obstacles reduces airflow disturbances, creating more stable conditions that favor the persistence of aerosol layers at specific altitudes.

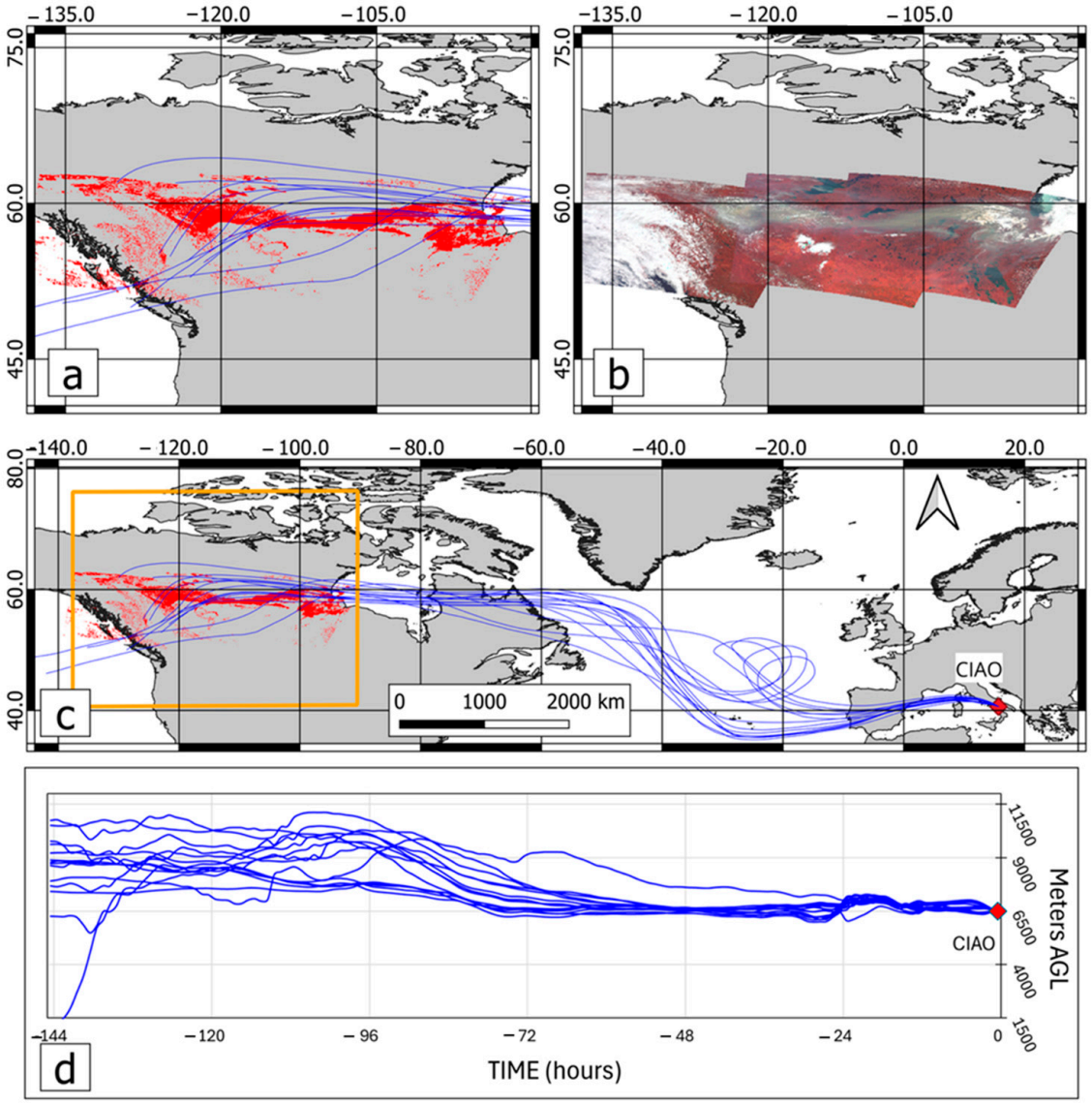

Figure 3. (**a**) Illustration of the smoke plume in red via an unsupervised k-means classification technique. Data for visualizing the smoke plume were obtained from the Sentinel-3 OLCI sensor during consecutive overpasses over Canada at 17:00, 18:00, and 19:00 UTC on 10 July 2024. (**b**) A false color representation using Sentinel-3 OLCI bands 17 (865 nm), 6 (560 nm), and 3 (490 nm), which effectively emphasizes the smoke in shades of gray and brown. (**c**) Integrates backward trajectories, illustrated in blue, computed with the HYSPLIT [54,55] model starting at 20:00 UTC on 16 July 2024 at an altitude of 6.5 km above CIAO, and tracing back for a period of six day. (**d**) Illustrates the trajectory heights as a function of time.

4. Discussion

4.1. Characterization of Smoke Plumes from a Local Wildfire

Continuous instrumental operation is essential for monitoring the onset of specific events and capturing their full evolution. In the case of small fires, where pyro-convection does not develop, the smoke plume tends to remain confined to the lower troposphere and is typically well mixed in the vicinity of the emission source due to weak vertical transport and local turbulence [20,56]. Moreover, the plume typically has a short lifetime due to deposition processes. Figure 4a shows the attenuated backscatter at 910 nm, measured by the CL51 ceilometer. At 16:30 UTC, an increase in aerosol signature is evident in the vertical interval 1.5–3.5 km. At this time, the solar activity is still strong enough to initiate and

sustain the development of a convective mixing layer (ML) driven by buoyant forces [57]. This turbulent motion is highly effective in vertically redistributing local air masses and aerosol particles, allowing the smoke emitted by the local fire to be transported upward to about 3 km. This mechanism facilitates the formation of elevated aerosol layers that can remain aloft for several hours. Additionally, at approximately 17:00 UTC, the smoke particles acted as cloud condensation nuclei and a thin cloud formed at 3 km (dashed rectangle in Figure 4a). As solar activity started to decrease, the turbulent processes within the mixing layer started to decay. Under these conditions, the mixing layer transits into a quite shallow nocturnal boundary layer (no longer characterized by turbulence), which is typically located below a residual layer characterized by a stratified and stable regime [58]. As a consequence, the elevated aerosol layer observed at approximately 3 km during night was no longer sustained by active convection but instead resided within the residual layer, where it remained decoupled from the surface. However, ceilometer observations indicate that, after 20:00 UTC, the bottom of the residual layer started to penetrate the underlying nocturnal layer following approximately the dashed white line reported in Figure 4a. This hypothesis is subsequently confirmed by the in situ measurements shown later in the paper.

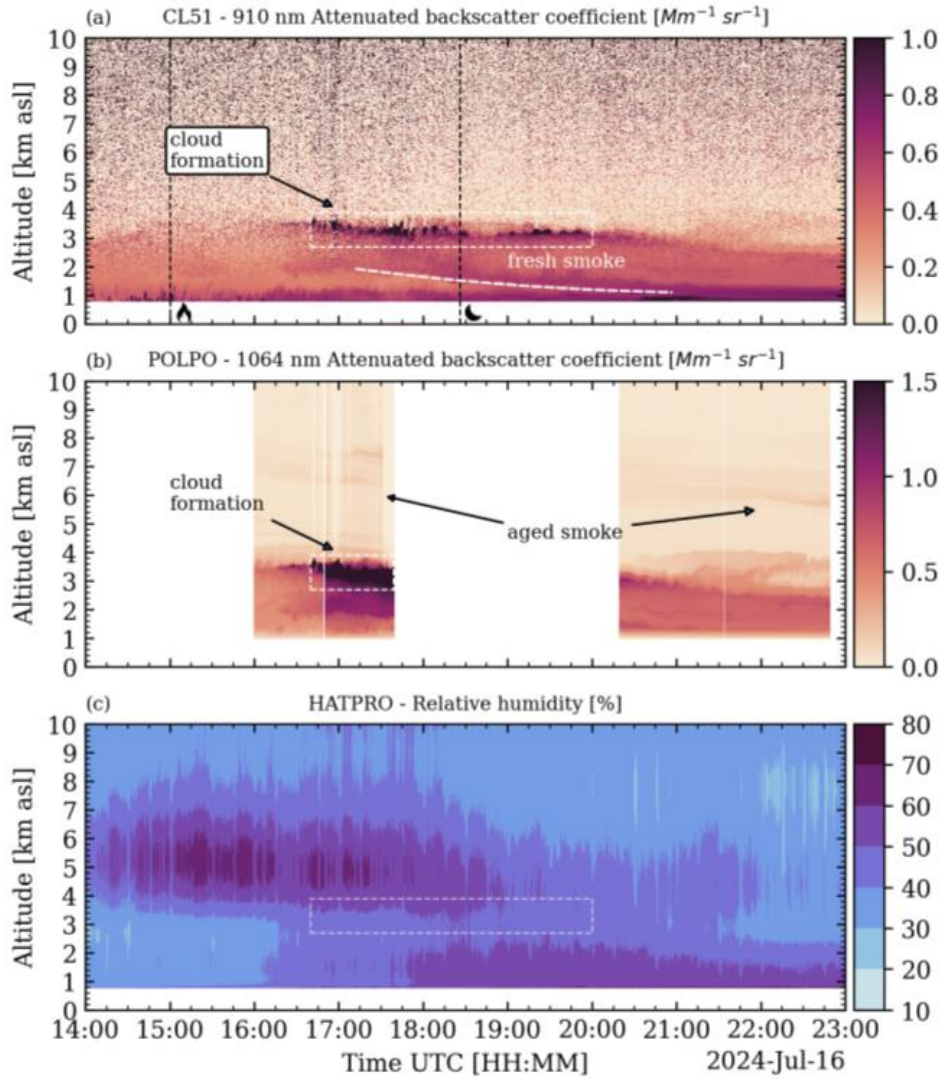

Figure 4. (**a**) Time series of CL51 attenuated backscatter coefficient; the area where cloud formation occurred is highlighted by a dashed rectangle; the dashed line shows the descending aerosols after 18:00 UTC. (**b**) POLPO attenuated backscatter coefficient at 1064 nm; Canadian fire layer visible above 7 km. (**c**) HATPRO relative humidity profiles measured on 16 July 2024 from 14:00 to 23:00 UTC. The area where cloud formation occurred is highlighted by a dashed rectangle.

Lidar measurements are not conducted continuously; therefore, they began only after the smoke was visually observed. The daytime measurements start at 15:59 UTC and are stopped at 17:29 UTC. Instead, the nighttime measurements start at 20:19 and finish at 22:50. The time–height evolution of the attenuated backscatter at 1064 nm (Figure 4b), unlike the CL51 measurements, shows a more detailed observation of the layers. Moreover, both daytime and nighttime lidar observations reveal the presence of aerosol layers at altitudes between 6 and 7 km. The microwave radiometer measurements (HATPRO G5) presented in Figure 4c reveal a significant increase in relative humidity after 16:00 UTC above 2.5 km, suggesting the onset of cloud formation. Indeed, in wildfire plumes, the smoke particles can absorb moisture when the ambient relative humidity is sufficiently high, increasing their size and causing them to become more spherical and effective at scattering light [59]. Moreover, smoke aerosols, particularly those rich in organic compounds, can act as CCN, leading to clouds' liquid droplet formation under favorable conditions [28].

The characterization of clouds formed from wildfires is widely studied in the literature, especially for larger-scale wildfires that produce substantial amounts of smoke and aerosols [60]. However, fewer studies have focused on clouds triggered by smaller-scale wildfires, which can still produce sufficient aerosols to initiate microphysical processes. In our case study, the ACTRIS classification of atmospheric particles indicates the presence of thin liquid water clouds from 16:30 to 20:00 UTC and above 3 km.

Figure 5 reports the ACTRIS cloud remote sensing products of the observed clouds, which have a maximum duration of 6 min; the cloud base height (Figure 5a, orange circle) in the range 3135–3465 m; the cloud top height (Figure 5a, blue circle) in the range 3255–3660 m; the liquid water content (Figure 5b) increasing with altitude and assuming values in the range 0.01–0.15 g m^{-3}; and the droplet effective radius (Figure 5c) increasing with altitude and assuming values in the range 4–5 µm. Consequentially, the clouds formed tend to exhibit smaller droplet sizes, leading to increased cloud reflectivity, or "cloud brightening" [29]. This phenomenon can result in net cooling, counteracting the warming effects typically associated with BC [40]. These clouds correspond to the peaks of the LWP measured by the HATPRO (Figure 5b, red line) for a total duration of about 20 min and are interrupted by cloud-free regions with aerosol particles affected by hygroscopic growth, given their high light-scattering efficiency and ambient relative humidity values of 40–60% measured by the HATPRO at the considered heights and time range.

In order to have a more comprehensive understanding of the observations, in situ measurements were also analyzed. These measurements provided important insights into the compositional properties of near-surface aerosol particles in order to assess the deposition of smoke at the ground. As already mentioned previously, CL51 ceilometer measurements (Figure 6a) show the presence of an aerosol layer progressively descending from an altitude of 1.5–3.5 km at 17:00. Furthermore, a thin layer reaches the surface after 20:00 UTC due to gravitational settling. ACSM (Aerosol Chemical Speciation Monitor) measurements (Figure 6b), on the other hand, show a peak in the organic component after 20:00 UTC, which indicates the deposition of the smoke particles on the ground. Indeed, the organic component is strongly correlated with biomass burning due to the specific nature of the emissions generated during the combustion process [60]. The temporal evolution of the Absorption Ångström exponent (AAE) and BC concentration (Figure 6c,d), as measured by the aethalometer, can be related to the presence of biomass burning associated with BC [61]. As shown, before 19:00 UTC, the aerosol particles are smaller, given the lower AAE values, and the biomass burning component is minimal, likely indicating that the observed aerosols are mainly from local vehicular traffic. Biomass burning particles, in contrast, tend to be larger due to incomplete combustion and hygroscopic growth. The subsequent increase in AAE aligns with the intrusion of smoke aerosols. In general, peaks in AAE correspond

to the presence of biomass burning particles. Furthermore, the relative humidity map (Figure 4c) consistently shows elevated values at ground level after 19:00 UTC. Under these conditions, the particles continue to grow in size due to hygroscopic processes. Indeed, organic aerosols, present in biomass burning, tend to be highly hygroscopic, meaning they readily absorb water in humid atmospheric conditions. This can lead to the growth of the particles and faster deposition.

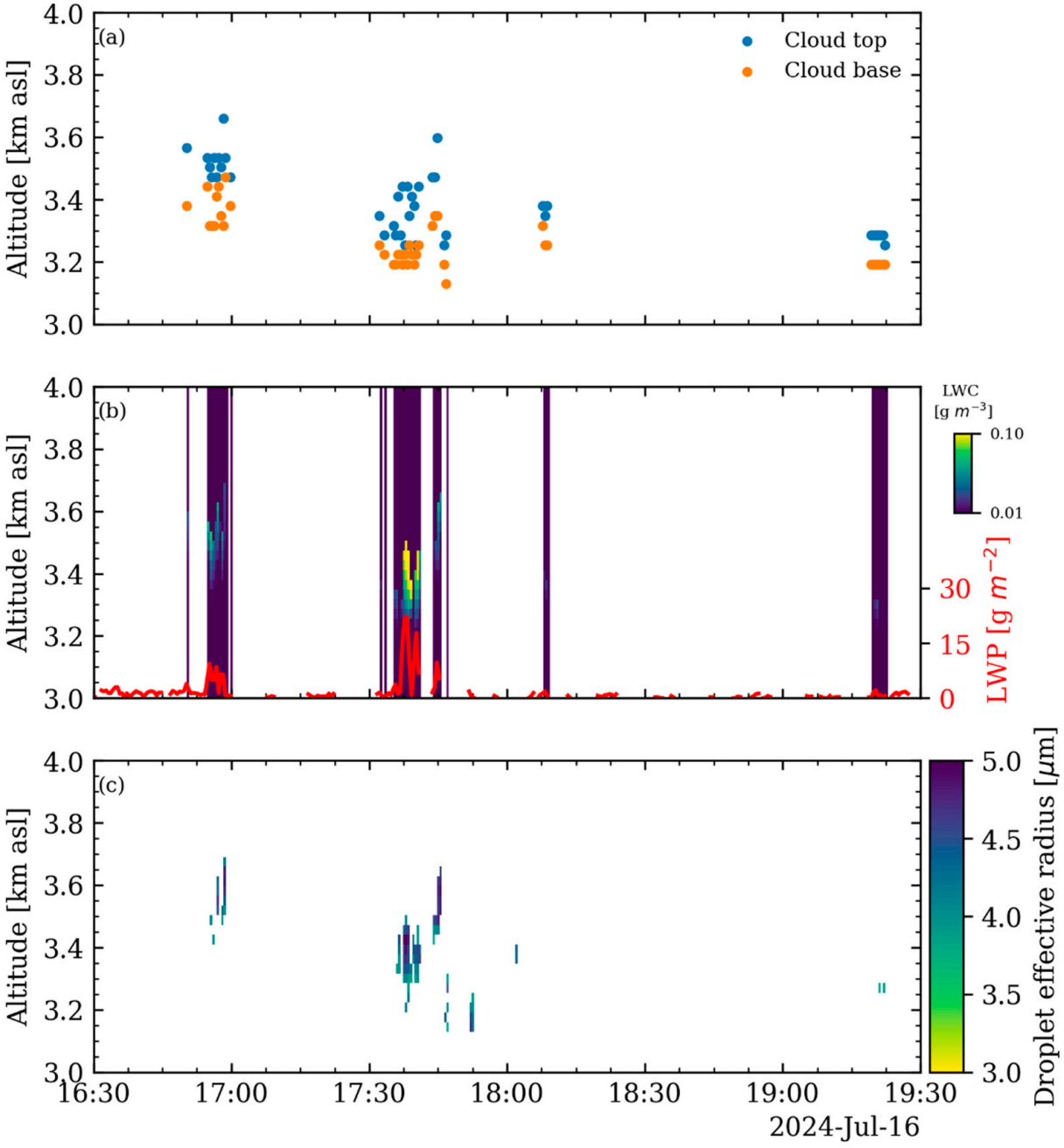

Figure 5. (**a**) Time series of cloud base height (a, orange circle), cloud top height (a, blue circle); (**b**) liquid water content (LWC) retrieved from MIRA 35, CL51 and HATPRO measurements of 16 July 2024 from 16:30 to 20:00 UTC using Cloudnet algorithms. The red line is the time series of cloud liquid water path (LWP) measured by the HATPRO. (**c**) Droplets' effective radius profiles, retrieved from MIRA 35, CL51 measurements of 16 July 2024 from 16:30 to 20:00 UTC using Cloudnet algorithms.

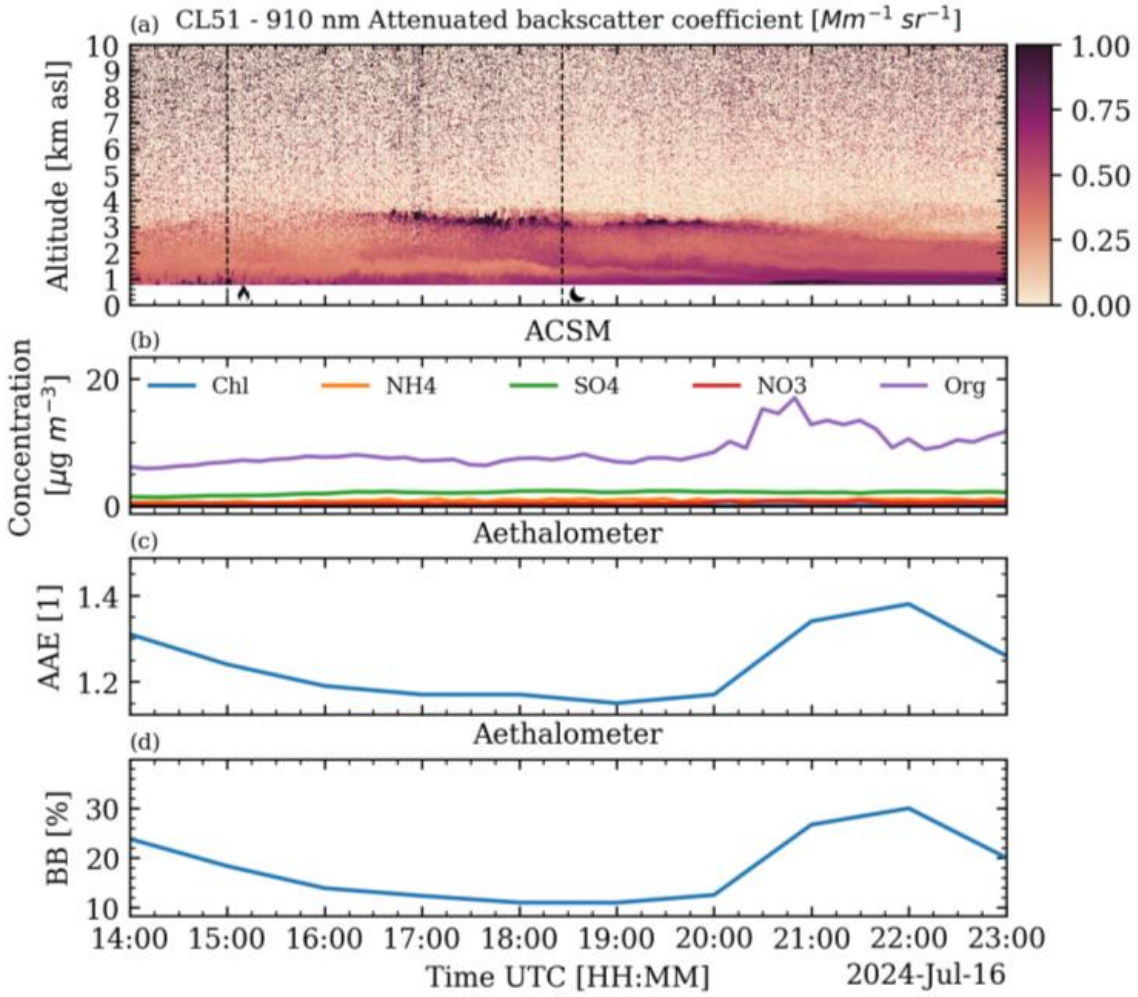

Figure 6. (**a**) Temporal evolution of CL51 attenuated backscatter coefficient. (**b**) ACSM concentration of aerosol chemical components. (**c**) Aethalometer Absorption Ångström exponent (AAE), (**d**) Aethalometer BC concentration, measured on 16 July 2024 from 14:00 to 23:00 UTC.

4.2. Optical Proprierties of Local Fire

To describe the temporal evolution of the optical properties of biomass burning aerosols, two distinct time intervals were analyzed. The first corresponds to daytime conditions (16:52–17:29 UTC), while the second is related to nocturnal conditions (21:19–21:34 UTC). The data were processed using the Single Calculus Chain (SCC), a centralized processing tool developed within the ACTRIS/EARLINET framework [38].

Figure 7 illustrates the vertical profiles of β, AEβ at 355–532, 355–1064, and 532–1064 nm, and PLDR at 355, 532 and 1064 nm, for the time interval 16:52–17:29 UTC. The altitude interval 3–3.5 km is the altitude region in which hygroscopic effects appear to be peaking. It is to be pointed out that, typically, particle hygroscopic behavior is dependent upon aerosol composition and may range from the hygrophobic to a strongly hygroscopic one, the latter with monotonic (smoothly varying) or deliquescent (step change) growth. The hygroscopicity of smoke particles dominated by carbonaceous organic material from biomass burning has been estimated to be typically characterized by relatively large enhancement factors [62].

The moderate values of PLDR from 1 to 3 km of 0.010 ± 0.002 at 532 nm and 0.091 ± 0.001 at 1064 nm suggest the presence of moderately irregular particles, likely indicative of freshly emitted biomass burning particles. In small fires, high temperatures are not typically reached, resulting in incomplete combustion. Consequently, the produced

particles tend to have a much more irregular shape compared to those generated by big fires [30,63]. Between 1 and 3 km, the AEβ values for the wavelength intervals 355–532 nm, 355–1064 nm, and 532–1064 nm are 1.79 ± 0.05, 1.01 ± 0.04, and 1.30 ± 0.04, respectively. These values suggest the dominance in the smoke plume of fine-mode particles. A noticeable decrease in AEβ occurs between 3 and 3.5 km, caused by the hygroscopic growth of particles. Specifically, we found values of 1.55 ± 0.04 for AEβ 355–532 nm, 0.92 ± 0.05 for AEβ 532–1064 nm, and 1.17 ± 0.05 for AEβ 355–532 nm. During this phase, the smoke particles absorb water vapor, ultimately increasing their size.

Furthermore, the hygroscopic growth leads to a slight reduction in the PLDR values (0.052 ± 0.001 at 532 nm and 0.050 ± 0.001 at 1064 nm) because, as the particles absorb humidity, they become more spherical. In the higher level (3–3.7 km), the lower PLDR values are a clear indication of the transition from irregularly shaped fresh biomass burning particles to more spherical, hygroscopically grown particles. This behavior is well documented in the literature, particularly in cases involving fire plumes interacting with high humidity environments [29]. Table 2 (in the first line) summarizes the smoke optical properties during the time interval when hygroscopic effects are more marked (16:50–17:29 UTC on 16 July 2024 from 3 to 3.5 km).

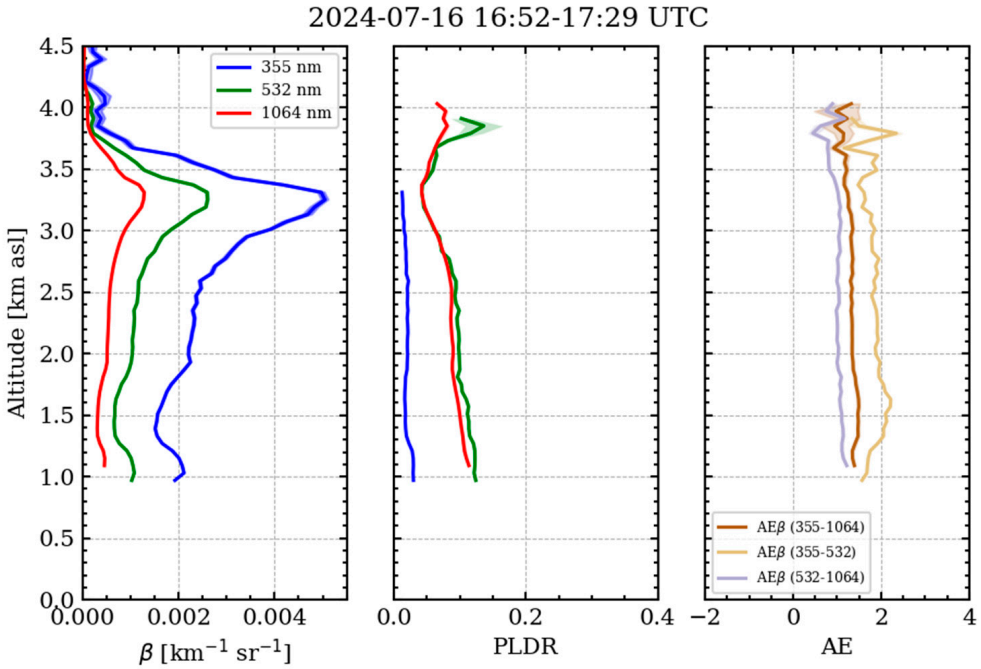

Figure 7. Vertical profiles of the aerosol optical parameters as measured in Potenza on 16 July 2024 from 16:50 to 17:29 UTC, with the multi-wavelength Raman lidar POLPO.

Table 2. The first line reports the values of AEβ at 355–532 nm, 532–1064 nm, and 355–1064 nm, and PLDR at 532 nm and 1064 nm from 3 to 3.5 km for 16 July 2024 from 16:50–17:29 UTC. The second line reports the values of LR at 532 nm, LR at 355 nm, AE at 355–532 nm, 532–1064 nm, and 355–1064 nm, and PLDR at 532 and 1064 nm, from 2.6 to 2.9 km for the 16 July 2024 from 21:19–21:34 UTC.

Date and Time	Alt a.s.l	LR 532	LR 355	LR 532/LR355	Aeβ 355–532	AEβ 355–1064	AEβ 532–1064	AEα 355–532	PLDR 532	PLDR 1064
16 July 2024, 16:50–17:29 UTC.	3–3.5	-	-	-	1.55 ± 0.04	1.17 ± 0.05	0.92 ± 0.05	-	0.052 ± 0.002	0.050 ± 0.001
16 July 2024, 21:19–21:34 UTC.	2.6–2.9	34.29 ± 2.8	45.60 ± 3.54	0.75 ± 0.09	1.21 ± 0.03	1.23 ± 0.03	1.22 ± 0.04	1.93 ± 0.05	0.067 ± 0.002	0.070 ± 0.001

From 21:19 to 21:34 UTC (Figure 8), the same smoke aerosol layer seen before is still visible, although with lower values of β (from 0.05 $km^{-1}sr^{-1}$ to 0.02 $km^{-1}sr^{-1}$ at 355 nm). The LR values are similar to those observed in other similar studies, and exhibit decreasing values with increasing wavelength. In particular, from 2.6 to 2.9 km, the LR at 355 nm (45.60 ± 3.54 sr) is significantly higher than that at 532 nm (34.29 ± 2.82 sr), a characteristic indicating the presence of fresh smoke particles [20,64]. This difference in LR at different wavelengths can be attributed to the size and composition of the aerosol particles. Freshly emitted biomass burning aerosols typically comprise a mix of organic and inorganic compounds, including BC, which exhibit strong light-absorption properties at shorter wavelengths, i.e., 355 nm. Consequently, the ratio of lidar ratios (RLR), defined as the ratio of LR532 to LR355 in our analysis, yields values below 1. Different studies have demonstrated that RLR values less than 1 are characteristic of fresh biomass burning aerosols, while values greater than or equal to 1 typically indicate aged biomass burning particles [21]. In this study the RLR is 0.75 ± 0.09 from 2.6 to 2.9 km.

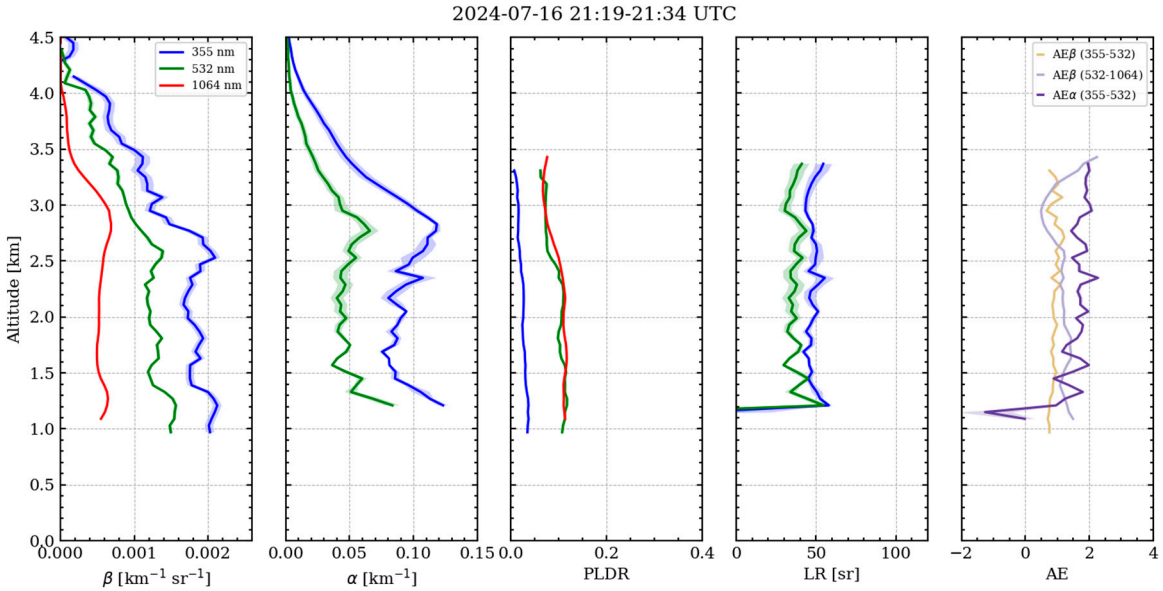

Figure 8. Vertical profiles of smoke optical parameters as measured in Potenza on 16 July 2024 from 21:19 to 21:34 UTC, with the multi-wavelength Raman lidar POLPO.

Furthermore, the persistence of high AE values during the nocturnal observations emphasizes the ongoing presence of these fine particles. Specifically, the extinction Ångström exponent (AEα) at 355–532 is 1.93± 0.05, AEβ 355–532 is 1.21 ± 0.03, AEβ 355–1064 is 1.23 ± 0.03, and AEβ 532–1064 is 1.22 ± 0.04.

Finally, the depolarization here is also lower in the upper layer. Indeed, from 1 to 2.5 km, the PLDR at 532 nm is 0.100 ± 0.003, and at 355 nm is 0.107 ± 0.002, while from 2.6 to 2.9 km it is 0.067 ± 0.002 at 532 nm and 0.070 ± 0.001 at 1064 nm. The values of the smoke optical properties during the time interval 21:19–21:34 UTC are summarized in the second line of Table 2 (second line).

4.3. Microphysical Properties of Local Fire

The β values at 1064, 532, and 355 nm and the aerosol extinction (α) coefficients at 355 and 532 were used to determine particle microphysical properties using regularization [65]. The inversion method with regularization [66,67] is based on the so-called Fredholm integral equations of the first kind. These equations describe the relation between aerosol optical and microphysical properties. Five integral equations are solved using Tikhonov's regularization method with constraints [68]. As the inverse problem is strongly

underdetermined, a number of a priori assumptions are necessary in the retrieval. Furthermore, only accurate aerosol optical property profiles can allow the retrieval of accurate microphysical properties [69].

In our study, the microphysical properties of the aerosol particles were retrieved for the vertical range 1.5–3 km, based on the optical parameter profiles measured between 21:19 and 21:34 UTC. In Figure 9a, we report the relative humidity measured by the HATPRO, due to its correlation with microphysical properties. The correlation between microphysical properties and humidity is crucial. Indeed, even when conditions are not favorable for cloud formation, aerosols produced by wildfires can undergo hygroscopic growth in the presence of high humidity levels, increasing their efficiency in absorbing radiation compared to those in dry air, with consequent influences on climate balance and air quality [29].

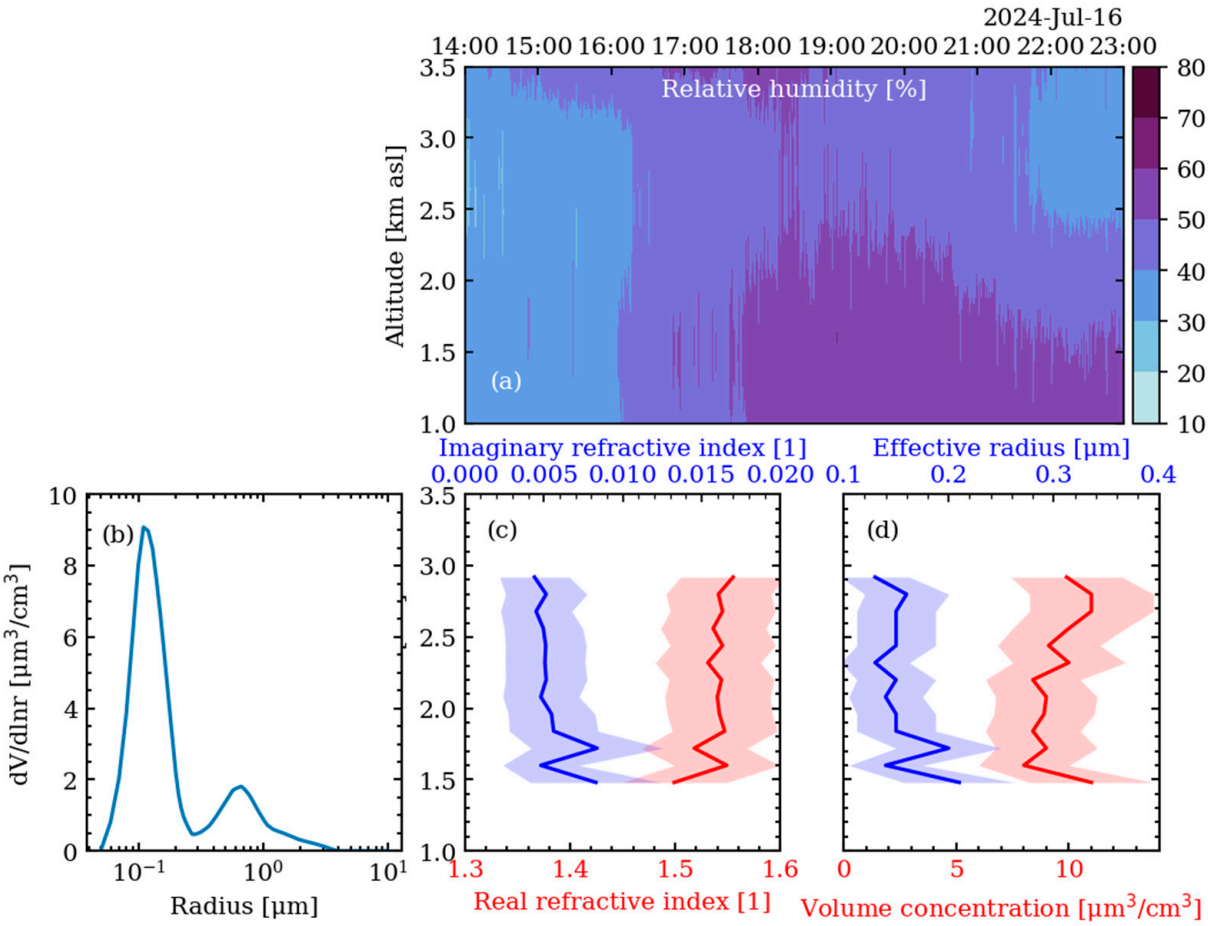

Figure 9. (**a**) Relative humidity measured by the HATPRO. (**b**) Particle volume size distribution at 2.08 km a.s.l. (**c**) Real (red) and imaginary (blue) part of refractive index. (**d**) Volume concentration (red) and effective radius (blue), retrieved from lidar measurements of 16 July 2024 from 21:19 to 21:34 UTC.

In this case, the particle volume size distribution at 2.08 km (Figure 9b) is bimodal and is dominated by the fine fraction around 0.1 µm. This distribution can be interpreted as a result of incomplete combustion processes and hygroscopic growth.

Particles at lower altitudes, swollen by humidity, exhibit a lower real refractive index, around 1.5 (Figure 9c, red line). This occurs because water, which has a low refractive index, dilutes the scattering power of the solid particles. In this scenario, the decrease in the real refractive index is not primarily due to the chemical composition of the particles, but rather to the increase in particle size and the presence of water. Therefore, the water

uptake alters the particle optical properties and significantly influences the interaction with radiation. Conversely, the hygroscopic growth significantly enhances the absorption of electromagnetic radiation by aerosol particles. Consequently, the values of the imaginary part of the refractive index are higher near the surface. As particles absorb moisture, their size increases, which in turn boosts their surface area and makes them more efficient at absorbing radiation, especially in the visible and infrared spectra. This process also modifies the particle's refractive index, as water has different optical properties than dry aerosol components, leading to a greater contrast between scattering and absorption (e.g., BC). Additionally, hygroscopic particles can exhibit a "lensing effect", where the water coating focuses radiation on the particle core, amplifying the absorption efficiency of light-absorbing substances like BC.

At higher altitudes, the aerosol particles tend to be smaller and drier due to the lower humidity levels, which results in less pronounced hygroscopic growth. These smaller particles exhibit a higher real part of the refractive index, as they are primarily composed of solid components such as sulphates or other secondary aerosols, which are highly effective at scattering radiation. The values range between 1.5 and 1.55 and are similar to those observed in other studies [63,70]. Conversely, the values of the imaginary part of the refractive index (Figure 9c, blue line) range from 0.004 to 0.009, and are lower up 1.8 km, as the absence of significant hygroscopic growth means they translate into smaller less-absorbing capabilities. The values are around 1.34 and are slightly higher than those found in another study [20].

The volume concentration (Figure 9d, red line), shown in Figure 9d, exhibits two distinct peaks, one near the surface and another around 2.6 km. These findings are consistent with the earlier lidar measurements, which detected multiple aerosol layers in this altitude range. The particle effective radius of particles (Figure 9d, blue line) near the surface is approximately 0.2 μm, larger than those at higher altitudes. The particles that have settled to the surface presumably underwent significant hygroscopic growth and continued to remain in a high-humidity environment. This is in agreement with what was previously stated from the analysis of the in situ and radiometer measurements. In contrast, above 2 km, low humidity inhibits hygroscopic growth. As a result, aerosols at these altitudes have a smaller effective radius of around 0.15 μm. Alados-Arboledas et al. [70] and Pereira et al. [63], in similar conditions, obtained a comparable range of effective radii, ranging from 0.13 to 0.17 μm and 0.14 to 0.19 μm, respectively. O'Neill et al. [71], based on sunphotometer observations, also found effective radii around 0.14 μm.

It is reasonable to assume that the smoke particles observed in the vertical range 1.5–3.5 km during the time interval 20:19–21:34 UTC, less than an hour after the observation of the thin liquid clouds above 3 km from 16:30 to 20:00 UTC, have the same microphysical properties as those that acted as CCN leading to the formation of these clouds. Therefore, the microphysical properties of smoke particles described above, together with those of clouds (Figure 4), can be of great interest to improve our understanding of liquid droplet formation on smoke particles, as well as to validate and improve the related parameterizations in atmospheric models [72–74]. Moreover, the same microphysical properties are key input parameters in the algorithms for estimating direct and indirect radiative effects of biomass burning aerosols [75,76].

4.4. Characterization of Smoke Plumes from Canadian Wildfires

Figure 10 shows the optical parameters retrieved starting from the POLPO lidar measurements from 22:19 to 22:50 UTC on 16 July 2024. The β profile clearly shows the presence of a biomass burning aerosol layer between 6 and 6.5 km originating from Canada, with a thin layer also visible between 7 and 8 km. From 6 to 6.5 km, the particle

depolarization values are very low, specifically 0.040 ± 0.003, significantly lower than those characterizing the smoke particles at lower levels (see Figure 6). Damiano et al. [77] reported similar values, ranging between 0.025 and 0.066, for long-range transported fire smoke layers generated by Canadian wildfires.

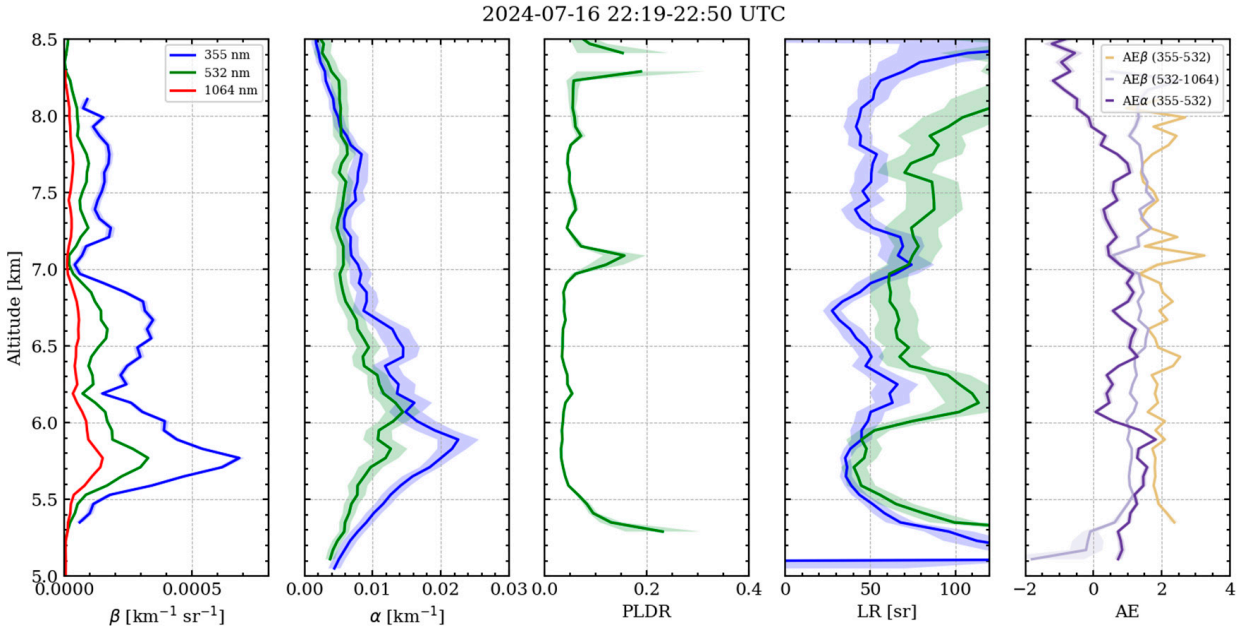

Figure 10. Vertical profiles of the aerosol optical parameters retrieved from lidar measurements provided by multi-wavelength Raman lidar POLPO in Potenza on 16 July 2024 from 22:19 to 22:50.

The comparison with the depolarization measured by [78] is also interesting. In this paper, LR values at the ACTRIS/EARLINET station in Leipzig indicate the presence of two layers related to a Canadian wildfire. The first layer, between 5 and 6.5 km, showed a PLDR at 532 nm of 0.03, very similar to what was measured in our case. Conversely, the layer at 15–16 km exhibited an incredibly high depolarization of approximately 0.22. Hu et al. [79] also showed an increase in PLDR with altitude in the biomass burning layer. Specifically in the layer at 5–6 km, the PLDR at 532 nm was below 0.03. Instead, between 6.5 and 9 km, the PLDR at 532 nm increased significantly up to 0.12 ± 0.02 at 532 nm.

This correlation between the PLDR of aged smoke and altitude is likely driven by altitude-dependent atmospheric factors, such as relative humidity (RH) and temperature, which influence the morphology of biomass burning particles during the aging process [80–82]. Furthermore, smoke reaching the stratosphere has typically enough energy to raise even larger and coarser particles. In our case, the back-trajectory analysis shows that the air masses always moved at altitudes between 6 and 7 km. In these cases, a balance is established between gravitational deposition and the heating of the air mass caused by the absorption of solar radiation by the soot particles. Unlike large-scale fires capable of injecting particles into the stratosphere, the energy associated with this event was likely insufficient to loft the largest and most irregular particles to high altitudes. Furthermore, in the upper troposphere, coarse particles tend to be efficiently removed during transport due to gravitational settling, unlike in the more stable stratosphere where larger particles can persist for longer periods [79]

As reported in previous studies [83–86] of aged wildfire events, the β of aged wildfire smoke particles in the troposphere presents a high wavelength dependence at 355 and 532 nm. Specifically, the β at 355 nm is higher. Instead, the corresponding extinction coefficient dependence on wavelength is considerably lower. Consequently, the LR at 532 nm is higher than the LR at 355 nm for aged smoke. For fresh smoke, instead, the

LR at 355 nm is generally greater than the LR at 532 nm. Specifically, in this case, the LR referring to the Canadian wildfire between 6 and 6.5 km is 82.26 ± 3.32 sr at 532 nm and 55.10 ± 2.29 at 355 nm. The RLR between 532 and 355 nm is 1.49 (Table 3). Conversely, in the local fire, the RLR is 0.75. Previous studies confirm that the RLR between 532 and 355 nm is usually greater than 1 for aged smoke particles and less than 1 for fresh smoke particles [20]. The AEβ 355–532 nm is 1.78 ± 0.14, for AEβ 532/1064 nm it is 1.41 ± 0.07, and for AEα 355–532 nm it is 1.11 ± 0.14, suggesting moderately smaller particles.

Table 3. Comparison between optical proprieties values calculated from 22:19 to 22:50 UTC at 6–6.5 km, and values calculated from 20:19 to 21:19 UTC at 2.6–2.9 km of LR at 532, LR at 355, AEβ at 355–532 nm and 532–1064, AEα at 355–532 nm, and PLDR at 532 and 1064.

Date and Time	Alt a.s.l. (km)	LR 532	LR 355	LR 532/LR355	AEβ 355–532	AEα 532–1064	AEα 355–532	PLDR 532
16 July 2024, 22:19–22:50 UTC.	6–6.5	82.26 ± 3.32	55.10 ± 2.29	1.49 ± 0.09	1.77 ± 0.13	1.41 ± 0.07	1.11 ± 0.14	0.040 ± 0.003
16 July 2024, 21:19–21:34 UTC.	2.6–2.9	34.29 ± 2.82	45.60 ± 3.54	0.75 ± 0.09	1.21 ± 0.03	1.21 ± 0.04	1.93 ± 0.09	0.067 ± 0.002

Additionally, Nicolae et al. [21] observed AEβ at the 355–532 nm wavelength interval is higher in the troposphere than in the stratosphere, and this is in agreement with the previous considerations referring to PLDR at 532 nm. The observed values align with other cases of tropospheric Canadian wildfires [87–89].

Table 3 shows the comparisons between the optical parameters measured for the fire from Canada and the local fire.

The microphysical inversion, shown in Figure 11, was also performed for the aerosol layer between 6 and 6.5 km. Figure 11a shows the relative humidity measured by the HATPRO and highlights how the air became drier in correspondence with the arrival of the plume from Canada.

The size distribution in Figure 11b exhibits a peak at 0.21 μm, which is noticeably larger than that observed in local fires, which was around 0.13 μm. However, a bimodal distribution is not present, as all particles are homogeneous. In general, smoke plumes originating from North American wildfires typically contain larger aerosol particles compared to those from fires in Brazil [90]. This difference is also influenced by the combustion phase; in North America, a considerable fraction of the burned material comes from smoldering subsurface layers, which enhances the emission of coarse particles. However, during the travel in the free troposphere, the coarse component is removed through sedimentation. Additionally. variations due to mixing with other aerosol types or interactions with humidity are minimal.

In Figure 11c, the real part of the refractive index is 1.5 and is consistent with previous measurements reported in the literature [91,92]. In contrast, the imaginary part is 0.09, almost twice as large as the one of local smoke particles. This is consistent with earlier findings regarding LR at 355 and 532 nm, where higher values of the complex refractive index correlate with increased absorption. This indicates that the BC content is significantly greater in large wildfires compared to smaller ones, where this contribution is almost negligible. In general, such high values of the imaginary part of the complex refractive index have rarely been measured [82], and this may be associated with the fact that, in the case under investigation, aging processes were limited. Indeed, during aging, the absorbing efficiency of aerosol particles decreases due to processes like coagulation, oxidation, and condensation of secondary compounds. As particles combine and grow in size, their surface area relative to their volume diminishes, reducing the efficiency of absorption [93]. The oxidation of BC and the formation of organic coatings further decrease absorption,

making the particles more reflective [93]. In addition, strong absorption is a characteristic feature of tropospheric smoke, where larger particles, typically responsible for scattering electromagnetic radiation, are removed. These exceptionally high values highlight the significant impact that such smoke plumes have on the Earth's energy balance.

In Figure 11d, the volume concentration measured is 1.2 $\mu m^3/cm^3$, while the surface concentration is 18 $\mu m^3/cm^2$, resulting in a numerical density of 48 cm^{-3}. Therefore, the concentrations are nine times lower compared to those observed during the local fire. The effective radius within this layer is 0.21 µm, which is larger than that measured for local biomass burning particles. In general, several studies [91,92] have reported effective radii of 0.15 µm for fresh smoke particles and between 0.3 and 0.4 µm for aged smoke. The microphysical inversion confirmed the results of the optical profile analysis; aging processes were of limited significance. Biomass burning aerosols observed in the troposphere after long-range transport are generally smaller than those measured in the stratosphere, due to the effective removal of larger particles during their transit through the troposphere. For example, ref. [94] measured effective radii of 0.17 µm in the troposphere and 0.32 µm in the stratosphere. Table 4 shows a comparison of the microphysical properties of the two biomass burning layers.

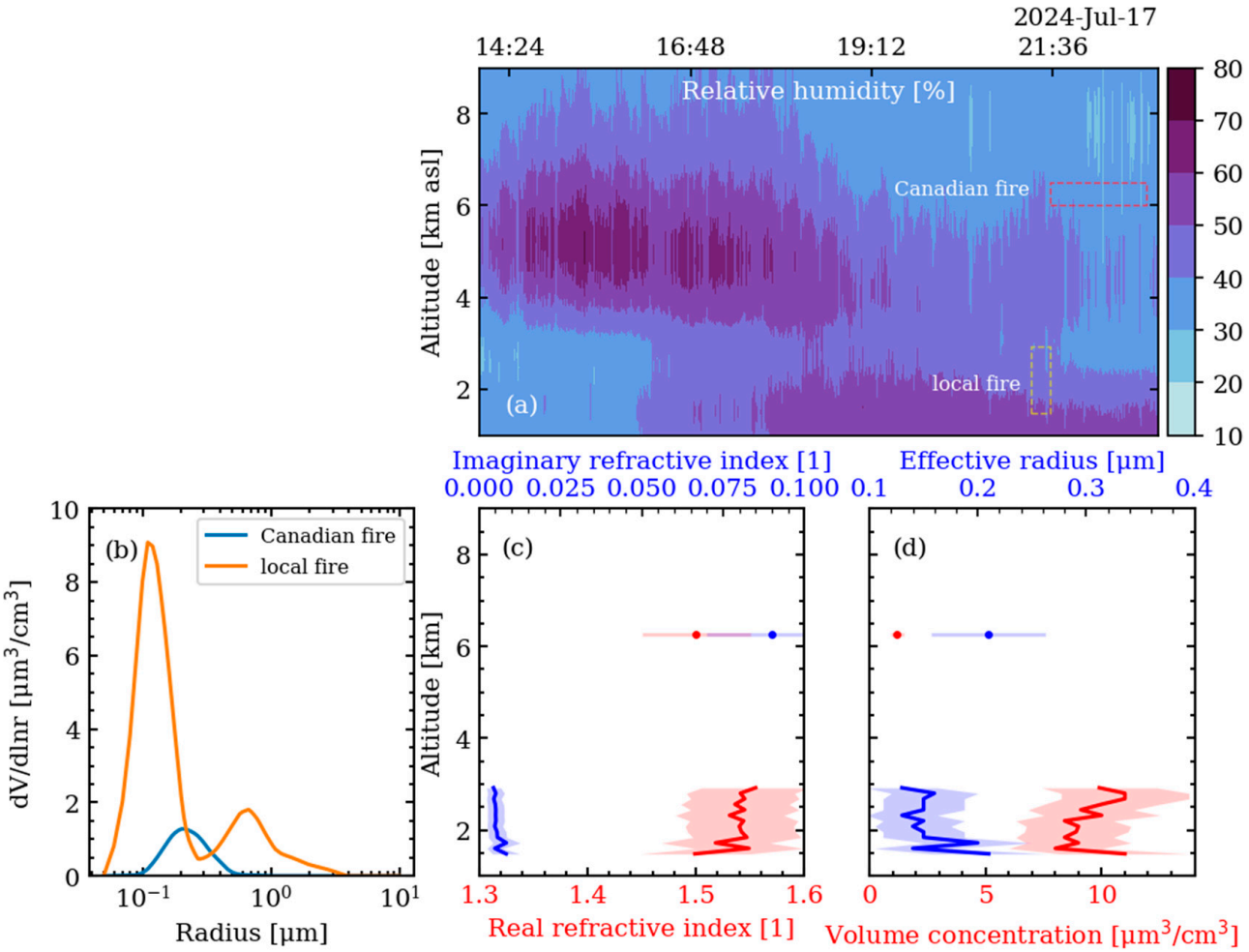

Figure 11. (**a**) Relative humidity measured by the HATPRO. (**b**) Particle volume size distribution for the local fire and the Canadian fire. (**c**) Real (red) and imaginary (blue) part of refractive index for the local fire and the Canadian fires. (**d**) Volume concentration (red) and effective radius (blue), for the local and the Canadian fire.

Table 4. Comparison between values calculated from 22:19 to 22:50 UTC at 6 to 6.5 km and values calculated from 20:19 to 21:19 UTC at 2.6–2.9 km of effective radius, volume concentration, and the real and imaginary parts of the refractive index.

Date and Time	Alt a.s.l. (km)	Reff (μm)	V (μm^3 cm^{-3})	mR	mi
16 July 2024, 22:19–22:50 UTC.	6–6.5	0.21 ± 0.04	1.2 ± 0.2	1.5 ± 0.1	0.09 ± 0.04
16 July 2024, 20:19–21:19 UTC.	2.6–2.9	0.14 ± 0.02	10.6 ± 2.1	1.5 ± 0.1	0.004 ± 0.002

5. Conclusions

This study demonstrates the critical value of a multi-instrumental approach for the comprehensive characterization of atmospheric aerosol properties and processes [95,96].

The dataset considered also offers an insight into understanding the lifecycle and atmospheric interactions of aerosols from a small-scale local fire and smoke transported from a Canadian forest fire.

The lidar measurements highlight the need for a more detailed representation of wildfires in climate models. While small fires, often undetectable by satellites, are increasing in frequency due to intensifying hot conditions, their aerosol properties differ significantly from those of major wildfires. Specifically, local fires exhibit markedly lower absorptive capacity, as evidenced by the imaginary part of the complex refractive index, which is 0.004 ± 0.002, compared to 0.09 ± 0.04 for Canadian smoke. Furthermore, due to their higher scattering efficiency and ability to promote cloud formation, these fires could potentially have a net cooling effect. Ignoring these distinctions in models could lead to overestimating the warming potential of wildfire emissions.

This study highlights the capabilities of the POLPO lidar, which uniquely characterizes aerosol optical properties using dual telescopes. Indeed, POLPO, with its high performance, is able to simultaneously characterize, from a microphysical point of view, a very thin intrusion of aerosol at 6 km and a very dense layer in the first 3 km.

The standardization of lidar operating procedures, quality assurance actions, and data processing within ACTRIS enables consistent and comparable characterization of such smoke events across Europe. This harmonization allows for the identification and analysis of local fire episodes with diverse atmospheric conditions and, consequently, supporting a continent-wide assessment of their climate relevance.

Furthermore, this study showcases the full potential of the ACTRIS Potenza site by synergistically using the different ACTRIS components. It further exemplifies that multi-disciplinary observation strategies are not only effective but necessary for advancement. Indeed, by integrating complementary techniques, it is possible to overcome the intrinsic limitations of individual instruments, enabling a more comprehensive investigation of atmospheric processes.

The results presented here underscore the advanced capabilities of the ACTRIS Potenza site, where co-located observations allow for the simultaneous characterization of near-surface, local smoke, and long-range transported smoke in the free troposphere. This integrated observational capacity is especially valuable for studying the highly variable nature of biomass burning aerosols and their interactions with the atmosphere. Such a multidisciplinary framework represents a fundamental step forward in the study of fire-related processes and will be increasingly important to clarify atmospheric mechanisms that remain poorly understood.

Finally, CIAO now has the capability to also perform lidar measurements of fluorescence, which is an invaluable tool in aerosol identification and typing [97]. Smoke particles exhibit a high degree of fluorescence, a property that can be used to distinguish them

from other aerosol types, including liquid water droplets that do not generate fluorescence [98,99]. This new technique will improve the capability of studying the interactions between biomass burning aerosols and clouds, particularly in scenarios where the underlying processes occur at smaller spatial scales, as demonstrated in this study.

Author Contributions: Conceptualization, B.D.R.; data curation, B.D.R., M.R., N.P., P.G.-C., T.L., F.C., A.F., E.R. and L.M.; formal analysis, B.D.R., M.R., I.V. and N.P.; investigation, B.D.R., N.P. and L.M.; writing—original draft, B.D.R.; writing—review and editing, M.M., A.A. (Aldo Amodeo), N.P., M.R., B.D.R., C.-A.P., G.D., P.D.G., D.S., L.M., D.A., C.C., I.G., A.G., E.L., F.M., R.M.P.A., M.V. and A.A. (Alberto Arienzo). All authors have read and agreed to the published version of the manuscript.

Funding: This research was funded by the ITINERIS, Italian Integrated Environmental Research Infrastructure-System (IR0000032, D.D. n.130/2022—CUPB53C22002150006) Funded by EU—Next Generation EU PNRR—Mission 4—Component 2—Investment 3.1., by the MUR (Italian Ministry of University and Research) that funded the work under PER-ACTRIS-IT (Potenziamento della com-ponente italiana della Infrastruttura di Ricerca Aerosol, Clouds and Trace Gases Research Infra-structure)—Avviso MUR D.D. n. 2595 del 24.12.2019 Piano Stralcio "Ricerca e Innovazione 2015–2017", through PIR01_00015, CUP B17E19000000007 and CIR01_00015, CUP F88I2000019000, and through the Joint Research Unit ACTRIS Italy, D. M. n. 571 del 21-6-2022, Fondo ordinario per gli enti e le istituzioni di ricerca (FOE) 2022 and D. M. n. 789 del 21-06-2023 Fondo ordinario per gli enti e le istituzioni di ricerca (FOE) 2023. This research was also funded by the Tech4You, Technologies for climate change adaptation and quality of life improvement, Funded by EU—Next Generation EU PNRR ambito di intervento "5. Climate, Energy and Sustainable Mobility" Missione 4—Compo-nente 2, "Dalla ricerca all'impresa" Investimento 1.5—CUP B83C22003980006, Repertorio contratto SIGLA: 19684/2022 and by the support of European Union through Horizon European project grant no. 101131261 IRISCC—Integrated Research Infrastructure Services for Climate Change Risks.

Data Availability Statement: The data used in this study are openly available through the ACTRIS-EARLINET data portal (https://data.earlinet.org, last access: 12 November 2024). They are also part of the ACTRIS-EARLINET 2024 Aerosol Optical Property Profiles over Potenza (Italy) dataset, generated by ACTRIS ARES Data Centre Unit, and accessible via the following DOI: https://doi.org/10.57837/cnr-imaa/ares/actris-earlinet/2024/pot/aerosol_optical_property_profiles accessed on 11 April 2025. For the cloud remote sensing component, the data are available at the Cloudnet data portal (https://cloudnet.fmi.fi, accessed on 11 April 2025) and on the ACTRIS data portal (https://data.actris.eu, accessed on 11 April 2025).

Acknowledgments: The authors acknowledge ACTRIS for all technical support and coordination, and in particularly the ACTRIS CLU and ARES Data Centre Units for providing cloud and aerosol remote sensing data, respectively. We acknowledge ECMWF for providing IFS model data, the MSI (MultiSpectral Instrument) onboard the Copernicus Sentinel-2 and the NOAA Air Resources Laboratory (ARL) for the provision of the HYSPLIT back trajectories.

Conflicts of Interest: The authors declare no conflictd of interest.

References

1. Johnston, F.H.; Henderson, S.B.; Chen, Y.; Randerson, J.T.; Marlier, M.; DeFries, R.S.; Kinney, P.; Bowman, D.M.J.S.; Brauer, M. Estimated global mortality attributable to smoke from landscape fires. *Environ. Health Perspect.* **2012**, *120*, 695–701. [CrossRef] [PubMed]
2. Reid, C.E.; Brauer, M.; Johnston, F.H.; Jerrett, M.; Balmes, J.R.; Elliott, C.T. Critical review of health impacts of wildfire smoke exposure. *Remote Sens.* **2016**, *124*, 1334–1343. [CrossRef] [PubMed]
3. Tian, L.; Wu, X.; Tao, Y.; Li, M.; Qian, C.; Liao, L.; Fu, W. Review of Remote Sensing-Based Methods for Forest Aboveground Biomass Estimation: Progress, Challenges, and Prospects. *Forests* **2023**, *14*, 1086. [CrossRef]
4. Bond, T.C.; Doherty, S.J.; Fahey, D.W.; Forster, P.M.; Berntsen, T.; DeAngelo, B.J.; Flanner, M.G.; Ghan, S.; Kärcher, B.; Koch, D.; et al. Bounding the role of black carbon in the climate system: A scientific assessment. *Remote Sens.* **2013**, *118*, 5380–5552. [CrossRef]

5. Curci, G.; Alyuz, U.; Barò, R.; Bianconi, R.; Bieser, J.; Christensen, J.H.; Colette, A.; Farrow, A.; Francis, X.; Jiménez-Guerrero, P.; et al. Modelling black carbon absorption of solar radiation: Combining external and internal mixing assumptions. *Atmos. Chem. Phys.* **2019**, *19*, 181–204. [CrossRef] [PubMed]
6. Turpin, B.J.; Lim, H.J. Species Contributions to PM2.5 Mass Concentrations: Revisiting Common Assumptions for Estimating Organic Mass. *Aerosol Sci. Technol.* **2001**, *35*, 602–610. [CrossRef]
7. Kuhlbusch, T.A.J.; Andreae, M.O. Black carbon formation during savanna fires: Seasonal variation of emission factors. *Sustainability* **2010**, *2*, 294–320. [CrossRef]
8. Popovicheva, O.B.; Persiantseva, N.M.; Kireeva, E.D.; Timofeev, M.A.; Shonija, N.K. Microstructure and physicochemical properties of black carbon particles from wildfire emissions. *Atmosphere* **2022**, *13*, 115. [CrossRef]
9. Liu, D.; Allan, J.D.; Whitehead, J.D.; Young, D.E.; Flynn, M.J.; Coe, H.; Beddows, D.C.S.; Taylor, J.W.; McFiggans, G.; Fleming, Z.L.; et al. Black-Carbon Absorption Enhancement in the Atmosphere Determined by Particle Mixing State. *Nat. Geosci.* **2017**, *10*, 184–188. [CrossRef]
10. Müller, D.; Mattis, I.; Ansmann, A.; Wandinger, U.; Ritter, C.; Kaiser, D. Multiwavelength Raman lidar observations of particle growth during long-range transport of forest-fire smoke in the free troposphere. *Geophys. Res. Lett.* **2007**, *34*, L05803. [CrossRef]
11. Andreae, M.O.; Merlet, P. Emission of trace gases and aerosols from biomass burning. *Glob. Biogeochem. Cycles* **2001**, *15*, 955–966. [CrossRef]
12. Romshoo, B.; Müller, T.; Pfeifer, S.; Saturno, J.; Nowak, A.; Ciupek, K.; Quincey, P.; Wiedensohler, A. Optical Properties of Coated Black Carbon Aggregates: Numerical Simulations, Radiative Forcing Estimates, and Size-Resolved Parameterization Scheme. *Atmosphere* **2021**, *12*, 12989. [CrossRef]
13. Li, Y.; He, C.; Liu, X.; Kang, H.; Zhang, Y.; Liu, J.; Yang, M.; Gong, X.; Zhu, T.; Martin, S.T. Liquid–Liquid Phase Separation Reduces Radiative Absorption by Aged Black Carbon Aerosols. *Commun. Earth Environ.* **2023**, *4*, 123. [CrossRef]
14. Papagiannopoulos, N.; Mona, L.; Amodeo, A.; D'Amico, G.; Gumà Claramunt, P.; Pappalardo, G.; Alados-Arboledas, L.; Guerrero-Rascado, J.L.; Amiridis, V.; Kokkalis, P.; et al. An automatic observation-based aerosol typing method for EARLINET. *Remote Sens.* **2020**, *12*, 1234. [CrossRef]
15. Baars, H.; Ansmann, A.; Ohneiser, K.; Althausen, D.; Engelmann, R.; Foth, A.; Heese, B.; Mattis, I.; Pappalardo, G.; Wandinger, U.; et al. The unprecedented 2017–2018 stratospheric smoke event: Decay phase and aerosol properties observed with the EARLINET. *Atmos. Chem. Phys.* **2019**, *19*, 15183–15198. [CrossRef]
16. Flannigan, M.D.; Stocks, B.J.; Turetsky, M.R.; Wotton, B.M. Implications of changing climate for global wildland fire. *Int. J. Wildland Fire* **2009**, *18*, 483–507. [CrossRef]
17. Val Martin, M.; Logan, J.A.; Kahn, R.A.; Leung, F.-Y.; Nelson, D.L.; Diner, D.J. Smoke injection heights from fires in North America: Analysis of 5 years of satellite observations. *Atmos. Chem. Phys.* **2010**, *10*, 1491–1510. [CrossRef]
18. Pappalardo, G.; Amodeo, A.; Apituley, A.; Comeron, A.; Freudenthaler, V.; Linné, H.; Ansmann, A.; Bösenberg, J.; D'Amico, G.; Mattis, I.; et al. EARLINET: Towards an advanced sustainable European aerosol lidar network. *Atmos. Meas. Tech.* **2014**, *7*, 2389–2409. [CrossRef]
19. Adam, M.; Nicolae, D.; Stachlewska, I.S.; Papayannis, A.; Balis, D. Biomass Burning Events Measured by Lidars in EARLINET—Part 1: Data Analysis Methodology. *Atmosphere* **2020**, *20*, 13905–13933. [CrossRef]
20. De Rosa, B.; Amato, F.; Amodeo, A.; D'Amico, G.; Dema, C.; Falconieri, A.; Giunta, A.; Gumà-Claramunt, P.; Kampouri, A.; Solomos, S.; et al. Characterization of Extremely Fresh Biomass Burning Aerosol by Means of Lidar Observations. *Remote Sens.* **2022**, *14*, 4984. [CrossRef]
21. Nicolae, D.; Nemuc, A.; Müller, D.; Talianu, C.; Vasilescu, J.; Belegante, L.; Kolgotin, A. Characterization of fresh and aged biomass burning events using multiwavelength Raman lidar and mass spectrometry. *J. Geophys. Res.* **2013**, *118*, 2956–2965. [CrossRef]
22. Chen, W.; Yan, L.; Ding, N.; Xie, M.; Lu, M.; Zhang, F.; Duan, Y.; Zong, S. Analysis of Aerosol Radiative Forcing over Beijing under Different Air Quality Conditions Using Ground-Based Sun-Photometers between 2013 and 2015. *Remote Sens.* **2016**, *8*, 510. [CrossRef]
23. Liang, Y.; Che, H.; Wang, H.; Zhang, W.; Li, L.; Zheng, Y.; Gui, K.; Zhang, P.; Zhang, X. Aerosols Direct Radiative Effects Combined Ground-Based Lidar and Sun-Photometer Observations: Cases Comparison between Haze and Dust Events in Beijing. *Remote Sens.* **2022**, *14*, 266. [CrossRef]
24. Andreae, M.O.; Rosenfeld, D.; Artaxo, P.; Costa, A.A.; Frank, G.P.; Longo, K.M.; Silva-Dias, M.A.F. Smoking rain clouds over the Amazon. *Science* **2004**, *303*, 1337–1342. [CrossRef] [PubMed]
25. Rosenfeld, D.; Zhu, Y.; Wang, M.; Zheng, Y.; Goren, T.; Yu, S. Aerosol-driven droplet concentrations dominate coverage and water of oceanic low-level clouds. *Science* **2019**, *363*, eaav0566. [CrossRef] [PubMed]
26. Ogawa, D.; Kanaya, Y.; Taketani, F.; Miyakawa, T.; Pan, X.; Kondo, Y. Hygroscopicity of Aerosol Particles and CCN Activity of Nearly Hydrophobic Particles in the Urban Atmosphere over Japan during Summer. *J. Geophys. Res. Atmos.* **2016**, *121*, 12000–12018. [CrossRef]

27. Massling, A.; Leinert, S.; Wiedensohler, A.; Covert, D. Hygroscopic Growth of Sub-Micrometer and One-Micrometer Aerosol Particles Measured during ACE-Asia. *Atmos. Chem. Phys.* **2007**, *7*, 3249–3259. [CrossRef]
28. Albrecht, B.A. Aerosols, cloud microphysics, and fractional cloudiness. *Science* **1989**, *245*, 1227–1230. [CrossRef] [PubMed]
29. Lohmann, U.; Feichter, J. Global indirect aerosol effects: A review. *Atmos. Chem. Phys.* **2005**, *5*, 715–737. [CrossRef]
30. Nessler, R.; Weingartner, E.; Baltensperger, U. Effect of Humidity on Aerosol Light Absorption and Its Implications for Extinction and the Single Scattering Albedo Illustrated for a Site in the Lower Free Troposphere. *J. Aerosol Sci.* **2005**, *36*, 958–972. [CrossRef]
31. Madonna, F.; Amodeo, A.; Boselli, A.; Cornacchia, C.; Cuomo, V.; D'Amico, G.; Giunta, A.; Mona, L.; Pappalardo, G. CIAO: The CNR-IMAA advanced observatory for atmospheric research. *Atmos. Meas. Tech.* **2011**, *4*, 1191–1208. [CrossRef]
32. Laurita, T.; Mauceri, A.; Cardellicchio, F.; Lapenna, E.; De Rosa, B.; Trippetta, S.; Mytilinaios, M.; Amodio, D.; Giunta, A.; Ripepi, E.; et al. CIAO observatory main upgrade: Building up an ACTRIS compliant aerosol in-situ laboratory. *Atmos. Meas. Tech. Discuss.* **2024**. *in review*.
33. De Rosa, B.; Mytilinaios, M.; Amodeo, A.; Colangelo, C.; D'Amico, G.; Dema, C.; Gandolfi, I.; Giunta, A.; Gumà-Claramunt, P.; Laurita, T.; et al. Observations of Saharan Dust Intrusions over Potenza, Southern Italy, During 13 Years of Lidar Measurements: Seasonal Variability of Optical Properties and Radiative Impact. *Remote Sens.* **2025**, *17*, 453. [CrossRef]
34. Laj, P.; Myhre, C.L.; Riffault, V.; Amiridis, V.; Fuchs, H.; Eleftheriadis, K.; Petäjä, T.; Salameh, T.; Kivekäs, N.; Juurola, E.; et al. Aerosol, Clouds and Trace Gases Research Infrastructure (ACTRIS): The European Research Infrastructure Supporting Atmospheric Science. *Atmosphere* **2020**, *11*, 1313. [CrossRef]
35. Freudenthaler, V. About the effects of polarising optics on lidar signals and the Δ90-calibration. *Atmos. Meas. Tech.* **2016**, *9*, 4181–4255. [CrossRef]
36. Freudenthaler, V. Optimized Background Suppression in Near Field Lidar Telescopes. In Proceedings of the 6th International Symposium on Tropospheric Profiling (ISTP), Leipzig, Germany, 14–20 September 2003.
37. Freudenthaler, V. Effects of Spatially Inhomogeneous Photomultiplier Sensitivity on Lidar Signals and Remedies. In Proceedings of the 22nd International Laser Radar Conference (ILRC 2004), Matera, Italy, 12–16 July 2004.
38. D'Amico, G.; Amodeo, A.; Mattis, I.; Freudenthaler, V.; Pappalardo, G. EARLINET Single Calculus Chain–technical–Part 1: Pre-processing of raw lidar data. *Atmos. Meas. Tech.* **2016**, *9*, 491–507. [CrossRef]
39. Madonna, F.; Amodeo, A.; D'Amico, G.; Pappalardo, G. A study on the use of radar and lidar for characterizing ultragiant aerosol. *Geophys. Res.* **2013**, *118*, 10056–10071. [CrossRef]
40. Gumà-Claramunt, P.; Madonna, F.; Amodeo, A.; Bauer-Pfundstein, M.; Papagiannopoulos, N.; Rosoldi, M.; Pappalardo, G. Giant Aerosol Observations with Cloud Radar: Methodology and Effects. *Remote Sens.* **2025**, *17*, 419. [CrossRef]
41. Granados-Muñoz, M.J.; García, S.; Mora, J.M.; Cuevas, E.; Alonso-Pérez, S.; Querol, X. Analysis of Four Years of Ceilometer-Derived Aerosol Backscatter Profiles in a Coastal Site of the Western Mediterranean. *Remote Sens.* **2021**, *13*, 2576. [CrossRef]
42. Chen, J.; Zeng, X.; Li, S.; Song, G.; Li, S. Water Vapor Correction in Measurements of Aerosol Backscatter Coefficients Using a 910 nm Vaisala CL51 Ceilometer. *Remote Sens.* **2025**, *17*, 2013. [CrossRef]
43. Jung, T.; Ruprecht, E.; Wagner, F. Determination of cloud liquid water path over the oceans from SSM/I data using neural networks. *J. Appl. Meteorol.* **1997**, *37*, 832844.
44. Solheim, F.; Godwin, J.; Westwater, E.; Han, Y.; Keihm, S.; Marsh, K.; Ware, R. Radiometric profiling of temperature, water vapor, and cloud liquid water using various inversion methods. *Radio Sci.* **1998**, *33*, 393–404. [CrossRef]
45. Illingworth, A.J.; Hogan, R.J.; O'Connor, E.J.; Bouniol, D.; Brooks, M.E.; Delanoé, J.; Donovan, D.P.; Eastment, J.D.; Gaussiat, N.; Goddard, J.W.F.; et al. Cloudnet: Continuous evaluation of cloud profiles in seven operational models using ground-based observations. *Bull. Am. Meteorol. Soc.* **2007**, *88*, 883–898. [CrossRef]
46. Tukiainen, S.; O'cOnnor, E.; Korpinen, A. CloudnetPy: A Python package for processing cloud remote sensing data. *J. Open Source Softw.* **2020**, *5*, 2123. [CrossRef]
47. Drinovec, L.; Močnik, G.; Zotter, P.; Prévôt, A.S.H.; Ruckstuhl, C.; Coz, E.; Rupakheti, M.; Sciare, J.; Müller, T.; Wiedensohler, A.; et al. The "dual-spot" Aethalometer: An improved measurement of aerosol black carbon with real-time loading compensation. *Atmos. Meas. Tech.* **2015**, *8*, 1965–1979. [CrossRef]
48. Sandradewi, J.; Prévôt, A.S.H.; Szidat, S.; Perron, N.; Alfarra, M.R.; Lanz, V.A.; Weingartner, E.; Baltensperger, U. Using Aerosol Light Absorption Measurements for the Quantitative Determination of Wood Burning and Traffic Emission Contributions to Particulate Matter. *Environ. Sci. Technol.* **2008**, *42*, 3316–3323. [CrossRef] [PubMed]
49. Fröhlich, R.; Cubison, M.J.; Slowik, J.G.; Bukowiecki, N.; Prévôt, A.S.H.; Baltensperger, U.; Schneider, J.; Kimmel, J.R.; Gonin, M.; Rohner, U.; et al. The ToF-ACSM: A portable aerosol chemical speciation monitor with TOFMS detection. *Atmos. Meas. Tech.* **2013**, *6*, 3225–3241. [CrossRef]
50. Middlebrook, A.M.; Bahreini, R.; Jimenez, J.L.; Canagaratna, M.R. Evaluation of composition-dependent collection efficiencies for the Aerodyne aerosol mass spectrometer using field data. *Aerosol Sci. Technol.* **2012**, *46*, 258–271. [CrossRef]

51. Borghetti, M.; Ferrara, A.; Moretti, N.; Nolè, A.; Pierangeli, D.; Ripullone, F.; Todaro, L. Caring for the Forests of an Inland Area in the Era of Climate Change: A Case Study of Basilicata, Southern Italy. *For. J. Silvic. For. Ecol.* **2024**, *21*, 10–36. [CrossRef]
52. Bai, M.; Yao, Q.; Wang, Z.; Wang, D.; Zhang, H.; Fang, K.; Guo, F. Driving Factors and Future Trends of Wildfires in Alberta, Canada. *Fire* **2024**, *7*, 419. [CrossRef]
53. Copernicus Atmosphere Monitoring Service (CAMS). CAMS on Air: Boreal Summer 24. Copernicus Atmosphere Monitoring Service, 2024. Available online: https://atmosphere.copernicus.eu/cams-air-boreal-summer-24 (accessed on 17 February 2025).
54. Rolph, G.; Stein, A.; Stunder, B. Real-time environmental applications and display system: READY. *Environ. Model. Softw.* **2017**, *95*, 210–228. [CrossRef]
55. Stein, A.F.; Draxler, R.R.; Rolph, G.D.; Stunder, B.J.B.; Cohen, M.D.; Ngan, F. NOAA's HYSPLIT atmospheric transport and dispersion modeling system. *Bull. Am. Meteorol. Soc.* **2015**, *96*, 2059–2077. [CrossRef]
56. Heilman, W.E. Atmospheric Turbulence and Wildland Fires: A Review. *Int. J. Wildland Fire* **2023**, *32*, 476–495. [CrossRef]
57. Garratt, J.R. *The Atmospheric Boundary Layer*; Elsevier: Amsterdam, The Netherlands, 1994.
58. LeMone, M.A.; Angevine, W.M.; Bretherton, C.S.; Chen, F.; Dudhia, J.; Fedorovich, E.; Katsaros, K.B.; Lenschow, D.H.; Mahrt, L.; Patton, E.G.; et al. 100 Years of Progress in Boundary Layer Meteorology. *Meteorol. Monogr.* **2019**, *59*, 9.1–9.85. [CrossRef]
59. Sicard, M.; Granados-Muñoz, M.J.; Alados-Arboledas, L.; Barragán, R.; Bedoya-Velásquez, A.E.; Benavent-Oltra, J.A.; Yela, M. Ground/space, passive/active remote sensing observations coupled with particle dispersion modeling to understand the inter-continental transport of wildfire smoke plumes. *Remote Sens. Environ.* **2019**, *232*, 111294. [CrossRef]
60. Noyes, K.T.J.; Kahn, R.A.; Limbacher, J.A.; Li, Z. Analyzing Canadian and Alaskan Wildfire Smoke Particle Properties and Their Evolution Using Satellite Observations. *Atmos. Chem. Phys.* **2022**, *22*, 10267–10287. [CrossRef]
61. Sinha, A.; George, I.; Holder, A.; Preston, W.; Hays, M.; Grieshop, A.P. Development of Volatility Distributions for Organic Matter in Biomass Burning Emissions. *Atmosphere* **2020**, *11*, 1234. [CrossRef] [PubMed]
62. Zhang, X.; Mao, M.; Yin, Y.; Tang, S. The Absorption Ångström Exponent of Black Carbon with Brown Coatings: Effects of Aerosol Microphysics and Parameterization. *Atmosphere* **2020**, *11*, 1234. [CrossRef]
63. Pereira, S.N.; Preißler, J.; Guerrero-Rascado, J.L.; Silva, A.M.; Wagner, F. Forest fire smoke layers observed in the free troposphere over Portugal with a multiwavelength Raman lidar: Optical and microphysical properties. *Sci. World J.* **2014**, *2014*, 421838. [CrossRef] [PubMed]
64. Veselovskii, I.; Kolgotin, A.; Griaznov, V.; Müller, D.; Wandinger, U.; Whiteman, D.N. Inversion with regularization for the retrieval of tropospheric aerosol parameters from multiwavelength lidar sounding. *Appl. Opt.* **2002**, *41*, 3685–3699. [CrossRef] [PubMed]
65. Müller, D.; Wandinger, U.; Ansmann, A. Microphysical particle parameters from extinction and backscatter lidar data by inversion with regularization. *Theory Appl. Opt.* **1999**, *38*, 2346–2357. [CrossRef] [PubMed]
66. Ansmann, A.; Müller, D. Lidar and Atmospheric Aerosol Particles. In *Lidar—Range-Resolved Optical Remote Sensing of the Atmosphere*; Weitkamp, C., Ed.; Springer: New York, NY, USA, 2005; pp. 105–141.
67. Tikhonov, A.N.; Arsenin, V.Y. *Solution of Ill-Posed Problems*; Wiley: New York, NY, USA, 1977.
68. Veselovskii, I.; Whiteman, D.N.; Kolgotin, A.; Andrews, E.; Korenskii, M. Demonstration of aerosol property profiling by multiwavelength lidar under varying relative humidity conditions. *J. Atmos. Oceanic Technol.* **2009**, *26*, 1543–1557. [CrossRef]
69. Veselovskii, I.; Dubovik, O.; Kolgotin, A.; Korenskiy, M.; Whiteman, D.N.; Allakhverdiev, K.; Huseyinoglu, F. Linear estimation of particle bulk parameters from multi-wavelength lidar measurements. *Atmos. Meas. Tech.* **2012**, *5*, 1135–1145. [CrossRef]
70. Alados-Arboledas, L.; Müller, D.; Guerrero-Rascado, J.L.; Navas-Guzmán, F.; Pérez-Ramírez, D.; Olmo, F.J. Optical and microphysical properties of fresh biomass burning aerosol retrieved by Raman lidar, and star-and sun-photometry. *Geophys. Res. Lett.* **2011**, *38*, L01807. [CrossRef]
71. O'Neill, N.T.; Eck, T.F.; Holben, B.N.; Smirnov, A.; Royer, A.; Li, Z. Optical properties of boreal forest fire smoke drived from Sun photometry. *J. Geophys. Res.* **2002**, *107*, AAC 6-1–AAC 6-19. [CrossRef]
72. Quinn, P.K.; Bates, T.S.; Coffman, D.J.; Covert, D.S. Influence of particle size and chemistry on the cloud nucleating properties of aerosols. *Atmos. Chem. Phys.* **2008**, *8*, 1029–1042. [CrossRef]
73. Kumar, P.; Sokolik, I.N.; Nenes, A. Parameterization of cloud droplet formation for global and regional models: Including adsorption activation from insoluble CCN. *Atmos. Chem. Phys.* **2009**, *9*, 2517–2532. [CrossRef]
74. Rose, D.; Nowak, A.; Achtert, P.; Wiedensohler, A.; Hu, M.; Shao, M.; Zhang, Y.; Andreae, M.O.; Pöschl, U. Cloud condensation nuclei in polluted air and biomass burning smoke near the mega-city Guangzhou, China—Part 1: Size-resolved measurements and implications for the modeling of aerosol particle hygroscopicity and CCN activity. *Atmos. Chem. Phys.* **2010**, *10*, 3365–3383. [CrossRef]
75. Fu, Q.; Liou, K.N. On the Correlated k-Distribution Method for Radiative Transfer in Nonhomogeneous Atmospheres. *J. Atmos. Sci.* **1992**, *49*, 2139–2156. [CrossRef]

76. Gu, Y.; Farrara, J.; Liou, K.N.; Mechoso, C.R. Parameterization of Cloud-Radiation Processes in the UCLA General Circulation Model. *J. Clim.* **2003**, *16*, 3357–3370. [CrossRef]
77. Damiano, R.; Amoruso, S.; Sannino, A.; Boselli, A. Lidar Optical and Microphysical Characterization of Tropospheric and Stratospheric Fire Smoke Layers Due to Canadian Wildfires Passing over Naples (Italy). *Remote Sens.* **2024**, *16*, 538. [CrossRef]
78. Haarig, M.; Ansmann, A.; Baars, H.; Jimenez, C.; Veselovskii, I.; Engelmann, R.; Althausen, D. Depolarization and lidar ratios at 355, 532, and 1064 nm and microphysical properties of aged tropospheric and stratospheric Canadian wildfire smoke. *Atmos. Chem. Phys.* **2018**, *18*, 11847–11861. [CrossRef]
79. Hu, Q.; Goloub, P.; Veselovskii, I.; Podvin, T. The characterization of long-range transported North American biomass burning plumes: What can a multi-wavelength Mie–Raman-polarization-fluorescence lidar provide? *Atmos. Chem. Phys.* **2022**, *22*, 5399–5414. [CrossRef]
80. Ohneiser, K.; Ansmann, A.; Engelmann, R.; Baars, H.; Althausen, D.; Pappalardo, G.; Wandinger, U.; Freudenthaler, V.; Heinold, B.; Müller, T.; et al. The unexpected smoke layer in the High Arctic winter stratosphere during MOSAiC 2019–2020. *Atmos. Chem. Phys.* **2021**, *21*, 15783–15798. [CrossRef]
81. Ansmann, A.; Engelmann, R.; Althausen, D.; Baars, H.; Pappalardo, G.; Wandinger, U.; Freudenthaler, V.; Heinold, B.; Müller, T.; Matvienko, G.; et al. Tropospheric and stratospheric wildfire smoke profiling with lidar. *Atmos. Chem. Phys.* **2021**, *21*, 9779–9803. [CrossRef]
82. Wandinger, U.; Müller, D.; Böckmann, C.; Althausen, D.; Matthias, V.; Bösenberg, J.; Weiß, V.; Fiebig, M.; Wendisch, M.; Stohl, A.; et al. Optical and Microphysical Characterization of Biomass-Burning and Industrial-Pollution Aerosols from Multiwavelength Lidar and Aircraft Measurements. *J. Geophys. Res. Atmos.* **2002**, *107*, LAC 7-1–LAC 7-20. [CrossRef]
83. Murayama, T.; Müller, D.; Wada, K.; Shimizu, A.; Sekiguchi, M.; Tsukamoto, T. Characterization of Asian Dust and Siberian Smoke with Multi-Wavelength Raman Lidar over Tokyo, Japan in Spring 2003. *Geophys. Res. Lett.* **2004**, *31*, L23103. [CrossRef]
84. Sugimoto, N.; Tatarov, B.; Shimizu, A.; Matsui, I.; Nishizawa, T. Optical Characteristics of Forest-Fire Smoke Observed with Two-Wavelength Mie-Scattering Lidars and a High-Spectral-Resolution Lidar over Japan. *SOLA* **2010**, *6*, 93–96. [CrossRef]
85. Hu, Q.; Goloub, P.; Veselovskii, I.; Bravo-Aranda, J.-A.; Popovici, I.E.; Podvin, T.; Haeffelin, M.; Lopatin, A.; Dubovik, O.; Pietras, C.; et al. Long-Range-Transported Canadian Smoke Plumes in the Lower Stratosphere over Northern France. *Atmos. Chem. Phys.* **2019**, *19*, 1173–1193. [CrossRef]
86. Papanikolaou, C.-A.; Giannakaki, E.; Papayannis, A.; Tombrou, M.; Mylonaki, M.; Soupiona, O. Optical Properties of Canadian Biomass Burning Particles over Europe Observed with CALIPSO and Ground-Based Lidar Systems. *EPJ Web Conf.* **2020**, *237*, 08016. [CrossRef]
87. Amiridis, V.; Balis, D.S.; Giannakaki, E.; Stohl, A.; Kazadzis, S.; Koukouli, M.E.; Zanis, P. Optical Characteristics of Biomass Burning Aerosols over Southeastern Europe Determined from UV-Raman Lidar Measurements. *Atmos. Chem. Phys.* **2009**, *9*, 2431–2440. [CrossRef]
88. Janicka, L.; Davuliene, L.; Bycenkiene, S.; Stachlewska, I.S. Long Term Observations of Biomass Burning Aerosol over Warsaw by Means of Multiwavelength Lidar. *Opt. Express OE* **2023**, *31*, 33150–33174. [CrossRef] [PubMed]
89. Müller, D.; Mattis, I.; Wandinger, U.; Ansmann, A.; Althausen, D.; Stohl, A. Raman Lidar Observations of Aged Siberian and Canadian Forest Fire Smoke in the Free Troposphere over Germany in 2003: Microphysical Particle Characterization. *J. Geophys. Res.* **2005**, *110*, D17201. [CrossRef]
90. Reid, J.S.; Hobbs, P.V. Physical and optical properties of smoke from individual biomass fires in Brazil. *J. Geophys. Res.* **1998**, *103*, 32013–32031. [CrossRef]
91. Müller, D.; Böckmann, C.; Kolgotin, A.; Schneidenbach, L.; Chemyakin, E.; Rosemann, J.; Znak, P.; Romanov, A. Microphysical Particle Properties Derived from Inversion Algorithms Developed in the Framework of EARLINET. *Atmos. Meas. Tech.* **2016**, *9*, 5007–5035. [CrossRef]
92. Di Girolamo, P.; De Rosa, B.; Summa, D.; Franco, N.; Veselovskii, I. Measurements of Aerosol Size and Microphysical Properties: A Comparison Between Raman Lidar and Airborne Sensors. *J. Geophys. Res. Atmos.* **2022**, *127*, e2021JD036086. [CrossRef]
93. Andreae, M.O.; Gelencser, A. Black carbon or brown carbon? The nature of light-absorbing carbonaceous aerosols. *Atmos. Chem. Phys.* **2006**, *6*, 3131–3148. [CrossRef]
94. Reid, J.S.; Kopp, H.; Higurashi, A.; Eck, T.F.; Zhang, J.; Li, Z.; Liu, Z.; Holben, B.N.; O'Neill, N.T.; Tsay, S.C. A review of biomass-burning aerosol properties in relation to atmospheric radiative forcing. *J. Geophys. Res.* **2005**, *110*, D10204. [CrossRef]
95. Summa, D.; Madonna, F.; Franco, N.; De Rosa, B.; Di Girolamo, P. Inter-Comparison of Atmospheric Boundary Layer (ABL) Height Estimates from Different Profiling Sensors and Models in the Framework of HyMeX-SOP1. *Atmos. Meas. Tech.* **2022**, *15*, 4153–4170. [CrossRef]
96. Summa, D.; Vivone, G.; Franco, N.; D'Amico, G.; De Rosa, B.; Di Girolamo, P. Atmospheric Boundary Layer Height: Inter-Comparison of Different Estimation Approaches Using the Raman Lidar as Benchmark. *Remote Sens.* **2023**, *15*, 1381. [CrossRef]
97. Reichardt, J.; Lauermann, F.; Behrendt, O. Fluorescence spectra of atmospheric aerosols. *EGUsphere* **2024**, *2024*, 1–52. [CrossRef]

98. Reichardt, J. Cloud and aerosol spectroscopy with Raman lidar. *J. Atmos. Ocean. Technol.* **2014**, *31*, 1946–1963. [CrossRef]
99. Reichardt, J.; Behrendt, O.; Lauermann, F. Spectrometric fluorescence and Raman lidar: Absolute calibration of aerosol fluorescence spectra and fluorescence correction of humidity measurements. *Atmos. Meas. Tech. Discuss.* **2022**, *2022*, 1–21. [CrossRef]